iScience

CellPress
OPEN ACCESS

Article

Analysis of the Active Species Responsible for Water Oxidation Using a Pentanuclear Fe Complex

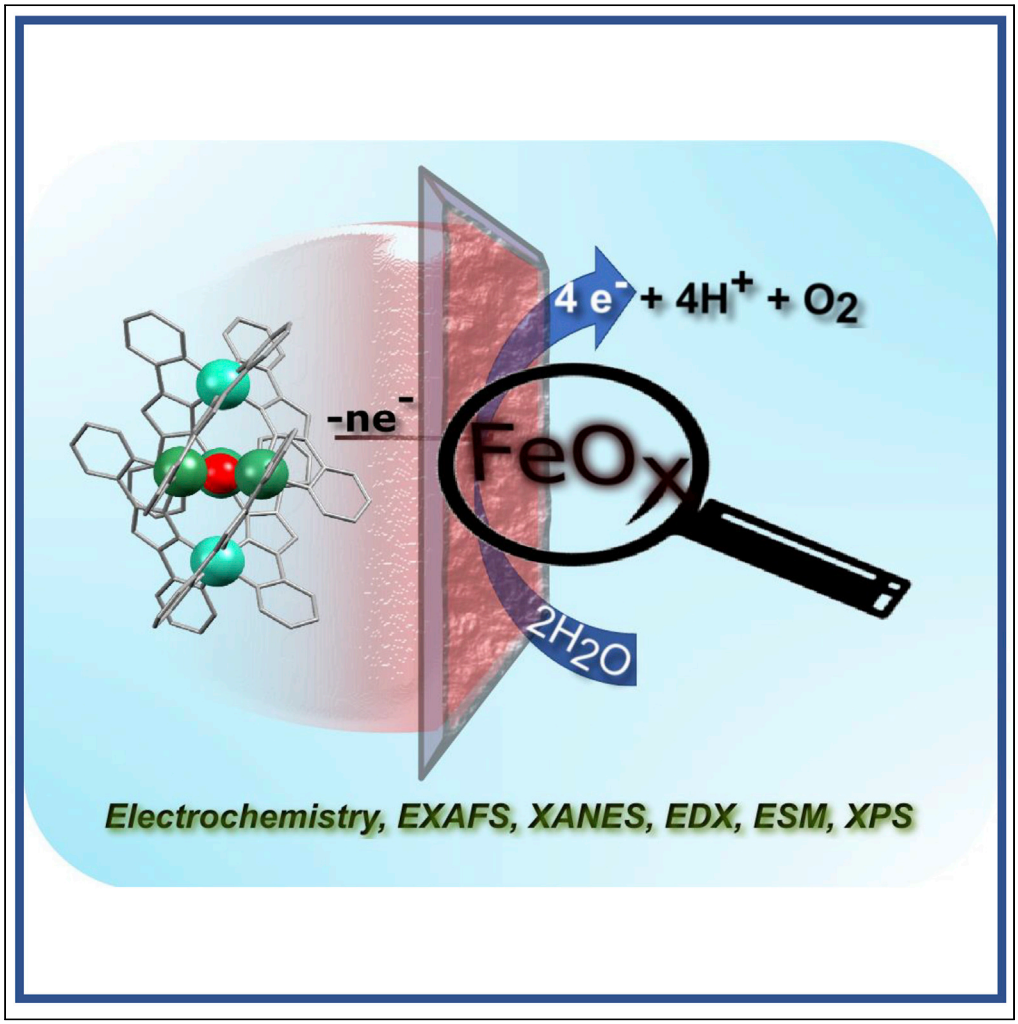

Primavera Pelosin, Marcos Gil-Sepulcre, Pablo Garrido-Barros, Dooshaye Moonshiram, Jordi Benet-Buchholz, Carolina Gimbert-Suriñach, Antoni Llobet

allobet@iciq.cat

HIGHLIGHTS

Electrochemical tools and XAS show the conversion of a Fe_5 complex into FeOx in H_2O

The FeOx generated adsorbs at the electrode and is responsible for the WO activity

The catalytic activity of FeOx depends on the conditions used for its generation

A thorough analysis is unavoidable to uncover the nature of the WO active species

Pelosin et al., iScience *23*, 101378
August 21, 2020
https://doi.org/10.1016/j.isci.2020.101378

iScience

CellPress
OPEN ACCESS

Article

Analysis of the Active Species Responsible for Water Oxidation Using a Pentanuclear Fe Complex

Primavera Pelosin,[1] Marcos Gil-Sepulcre,[1] Pablo Garrido-Barros,[1] Dooshaye Moonshiram,[2] Jordi Benet-Buchholz,[1] Carolina Gimbert-Suriñach,[1] and Antoni Llobet[1,3,4,*]

SUMMARY

Water splitting with sunlight is today one of the most promising strategies that can be used to start the imperatively needed transition from fossil to solar fuels. To achieve this, one of the key reactions that need to be mastered is the electrocatalytic oxidation of water to dioxygen. Great developments have been achieved using transition metal complexes mainly based on Ru, but for technological applications it is highly desirable to be able to use earth-abundant transition metals. The intrinsic chemistry of first row transition metals and in particular the lability of their M-L bonds in water imposes serious challenges for the latter to work as real molecular catalysts. The present work addresses this issue based on a molecular pentanuclear Fe_5 complex and describes the different protocols and tests that need to be carried out in order to identify the real active species, responsible for the generation of dioxygen.

INTRODUCTION

One of the main threats on the lifestyle of our modern societies is the increased global warming effect caused through the emission of greenhouse gases. The massive burning of fossil fuels over the course of the past decades has resulted in an alarming increase in carbon dioxide concentrations responsible for the global climate change and concomitant environmental issues.

It is thus extremely urgent to replace fossil fuels by new energy conversion schemes based on clean and environmentally respectful fuels. A potential option is the production of H_2 through water splitting with sunlight (hν-WS) as indicated in Equation (1).

$$2H_2O_{(l)} + h\nu \rightarrow O_{2(g)} + 2H_{2(g)} \quad \text{(Equation 1)}$$

$$2H_2O_{(l)} \rightarrow O_{2(g)} + 4H^+_{(aq)} + 4e^- \quad E^o = 1.23\ V\ vs.\ NHE\ at\ pH\ 0.0 \quad \text{(Equation 2)}$$

$$2H^+_{(aq)} + 2e^- \rightarrow H_{2(g)} \quad E^o = 0.0\ V\ vs.\ NHE\ at\ pH\ 0.0 \quad \text{(Equation 3)}$$

Hydrogen generated in this manner is termed solar fuel. Furthermore, hν-WS is also termed as artificial photosynthesis (Grätzel, 1981; Berardi et al., 2014; Lewis, 2016; Nocera, 2017; Roger et al., 2017; Guan et al., 2018) because there are a number of analogies with this reaction and the one that occurs in the natural photosynthesis summarized in Equation (4) (Nelson and Ben-Shem, 2004; McEvoy and Brudvig, 2006; Croce and van Amerongen, 2014).

$$6CO_{(g)} + 6H_2O_{(l)} + h\nu \rightarrow C_6H_{12}O_{6(aq)} + 6O_{2(g)} \quad \text{(Equation 4)}$$

From a chemical perspective these analogies include:

(1) Both reactions are thermodynamically uphill, driven by sunlight and require the participation of light harvesting agents that can transfer the sun's energy into high-energy-density chemicals such as carbohydrates or H_2; (2) both processes need catalysts to speed up the redox reactions; and (3) the water oxidation reaction occurs in an identical fashion in natural photosynthesis and in hν-WS. In the former case a tetramanganese cluster located in photosystem II (PSII) is employed as a catalyst to speed up the water to dioxygen reaction.

[1]Institute of Chemical Research of Catalonia (ICIQ), The Barcelona Institute of Science and Technology (BIST), Avinguda Països Catalans 16, Tarragona 43007, Spain

[2]Instituto Madrileño de Estudios Avanzados en Nanociencia (IMDEA-Nanociencia), Calle Faraday 9, Madrid 28049, Spain

[3]Departament de Química, Universitat Autonoma de Barcelona, Cerdanyola del Valles, Barcelona 08193, Spain

[4]Lead Contact

*Correspondence: allobet@iciq.cat

https://doi.org/10.1016/j.isci.2020.101378

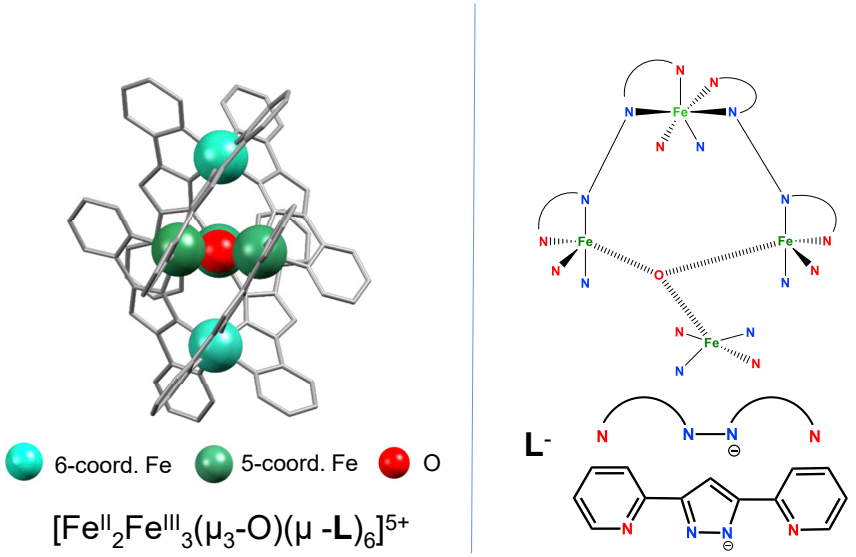

Figure 1. Crystal Structure of Fe_5^{5+}

Left, ball and stick drawing of the cationic part of $[Fe^{II}_2Fe^{III}_3]^{5+}$. The Fe centers and the oxygen atoms are represented as green and red spheres, respectively. The two Fe(II) centers are situated in the equatorial plane of the bipyramid. The bpp^- ligand is represented with gray sticks. H atoms are not drawn for simplicity reasons. Top right, partial representation of the upper part of bipyramidal structure of the Fe_5^{5+} complex showing only two of the six bpp^- ligands (for simplicity purposes) bridging axial and equatorial Fe centers. Bottom right, drawn structure of the bpp^- (L^-) ligand and its representation using arcs connected with N.

The water oxidation reaction has long been regarded as a major bottleneck that ought to be solved to be able to develop devices based on hv-WS. However, during the last decade, a large degree of knowledge has been generated based on both oxide materials (Smith et al., 2013; McCrory et al., 2015; Godwin et al., 2018) and molecular transition metal complexes (Blakemore et al., 2015; Garrido-Barros et al., 2017; Matheu et al., 2019a, 2019b).

In this context, the molecular water oxidation catalysis field has experienced a significant progress over the last 10 years powered by the promise of generating sustainable carbon neutral fuels based on water splitting (Lewis and Nocera, 2006, 2007; Llobet and Meyer, 2011). A particularly noteworthy contribution has been the development of water oxidation catalysts containing molecular Ru complexes owing to the high degree of understanding of their performance at a molecular level. This has been achieved thanks to a thorough description of their reactivity, electrochemical and spectroscopic properties, as well as a detailed characterization of their reaction intermediates, all combined with complementary computational models (Ellis et al., 2010; Radaram et al., 2011; Sala et al., 2014; Matheu et al., 2015; Keidel et al., 2017).

It would be very convenient to use non-toxic earth-abundant transition metal complexes such as Fe-based catalysts as water oxidation catalyst (WOCs) for the generation of technologically useful devices. Few Fe-based WOCs have been reported so far, but most of them are unfortunately not free from controversy since in most of the cases the real active catalytic species is most likely the corresponding oxide rather than the initial molecular complex (Hoffert et al., 2013; Pattanayak et al., 2017). Therefore, rigorous analysis of the active species is essential in order to achieve meaningful information of the catalytic species, not only in water oxidation but in the field of molecular electrocatalysis (Kaeffer et al., 2016; Folkman et al., 2018).

The present work analyzes the water oxidation catalysis initially associated to the complex $[Fe^{II}_4Fe^{III}(\mu_3\text{-O})(\mu\text{-bpp})_6]^{3+}$, from now on labeled as $[Fe^{II}_4Fe^{III}]^{3+}$ or Fe_5^{3+} (Okamura et al., 2016), where bpp^- is the anionic tetradentate dinucleating bridging ligand 3,5-bis(2-pyridyl)pyrazolato; see Figure 1 for a drawing of its two electron oxidized derivative. The transformation of the metal complex into the corresponding oxide is a major concern here since it precludes the correlation of reactivity with the catalytic process and thus becomes a futile exercise. Such exercises could generate misleading information in the water oxidation field.

This manuscript summarizes the main critical tests that need to be carried out to prove the molecular nature of the catalytic processes using $\mathbf{Fe_5}^{3+}$ but that it obviously can be extended to other iron complexes as well as to other earth-abundant first row transition metal complexes.

RESULTS

$\mathbf{Fe_5}^{n+}$ Synthesis, Structure, and Redox Electronic Properties in MeCN

The reaction of $Fe(SO_4)\cdot 7H_2O$ and bpp^- in MeOH in an open atmosphere gives rise to the formation of a pentanuclear complex $[Fe^{II}_4Fe^{III}(\mu_3\text{-}O)\,(\mu\text{-}bpp)_6]^{3+}$, $\mathbf{[Fe^{II}_4Fe^{III}]^{3+}}$ or $\mathbf{Fe_5}^{3+}$, with a relatively high isolated yield of ~72%. Although UV-vis spectroscopy shows that the reactions proceed quantitatively (see Figure S3), the decrease in the isolated yield is due to the crystallization process and the follow-up operations needed to isolate a pure solid.

Complex $\mathbf{Fe_5}^{3+}$ can be cleanly and successively oxidized by two one-electron processes in MeCN reaching the high oxidation state complex $[Fe^{II}_2Fe^{III}_3(\mu_3\text{-}O)\,(\mu\text{-}bpp)_6]^{5+}$, $\mathbf{[Fe^{II}_2Fe^{III}_3]^{5+}}$ or $\mathbf{Fe_5}^{5+}$, whose crystal structure is shown in Figure 1. In the structure, the metal centers are situated at the vertex of a triangular bipyramid where the bpp^- acts as a bridging ligand between the axial and equatorial Fe, whereas the oxido group bridges the three Fe sites situated in the equatorial plane. The axial Fe sites are hexacoordinated (CN_6) with a distorted O_h symmetry, whereas the equatorial ones are pentacoordinated (CN_5) with a distorted C_{2v} symmetry. This crystal structure is very similar to the previously reported one for $\mathbf{Fe_5}^{3+}$ complex (Okamura et al., 2016), except for a slightly shorter Fe-O and Fe-N distances as expected (Figure S1 and Table S1) (Sreerama and Pal, 2004).

It is important to realize here that the quantitative yield of this reaction implies that the pentanuclear structure is especially stable from a thermodynamic perspective given the large number of complexes that can be potentially formed by mixing the bpp^- ligand and the iron $[Fe^{II}(H_2O)_6]^{2+}$ (obtained from the dissolution of iron sulfate in water), as shown in Figure S2. These potential complexes range from simple mononuclear complexes with different number of bbp^- ligands bonded to the Fe center to dinuclear, polynuclear, etc., again with different numbers of coordinated bpp^- ligands attached to Fe. The formation of $\mathbf{Fe_5}^{3+}$ as the only complex generated in this reaction points to a scenario whereby the Fe-N bond is forming and breaking easily in agreement with the lability of high spin Fe(II) and Fe(III) complexes (Helm and Merbach, 2006). This is exemplified in Figure S2 where the first Fe complexes that will most likely be made upon mixing Fe(II) and bpp^- are shown. The *fac*-$[Fe(L)_3]^-$ complex will end up acting as a capping group for the final $\mathbf{Fe_5}^{3+}$ complex. Only the $[Fe(L)\,(H_2O)_4]^+$ and the *cis,cis*-$[Fe(L)_2(H_2O)_2]$ complexes will have the proper ligand geometrical coordination so that they can lead to the formation of *fac*-$[Fe(L)_3]^-$ without the need of additional ligand rearrangements. All the other complexes will need to rearrange, and thus Fe-N bonds will have to be broken and made anew to be able to lead to *fac*-$[Fe(HL)_3]^-$. Thus, all the potential complexes generated at the initial stages of the synthesis will reorganize in order to converge to the most thermodynamically stable complex, which is, in this case, $\mathbf{Fe_5}^{3+}$. A parallel phenomenon also occurs with other metal complexes such as Mn that can achieve a similar structural arrangement with bpp^-, such as $[Mn^{II}_4Mn^{III}(\mu\text{-}bpp)_6(\mu_3\text{-}O)]^{3+}$, $\mathbf{Mn_5}^{3+}$, and also with related linearly arranged tetranucleating ligands (Bao et al., 2010; Romain et al., 2011).

Although the $\mathbf{Fe_5}^{3+}$ is relatively stable in solution at low concentrations of water, the corresponding Mn analog, the $\mathbf{Mn_5}^{3+}$, decomposes almost immediately to generate the free ligand and $[Mn(H_2O)_6]^{2+/3+}$ (Romain et al., 2011). This indicates the capacity of H_2O to compete for the first coordination sphere of the Mn center, so that once a water molecule coordinates to a Mn center the whole structure collapses losing the stability provided by the pentanuclear arrangement.

In MeCN as solvent, the $\mathbf{Fe_5}^{n+}$ complex is a very rich molecule from a redox perspective accessing six different oxidation states ranging from $[Fe^{II}_5(\mu_3\text{-}O)\,(\mu\text{-}bpp)_6]^{2+}$, $\mathbf{Fe_5}^{2+}$, where all the iron centers have oxidation state II up to $[Fe^{III}_5(\mu_3\text{-}O)\,(\mu\text{-}bpp)_6]^{7+}$, $\mathbf{Fe_5}^{7+}$, where now all Fe centers have oxidation state III. All the oxidation states can be accessed by successive one electron electrochemically quasireversible processes, as can be observed in the CV in Figure 2 and in agreement with a previous report (Gouré et al., 2016) (see Figure S4 and Table S2 for further details). All CVs in this work are carried out using a glassy carbon (GC) electrode as a working electrode, an Ag^+/Ag (0.01 M) as reference electrode and a Pt disk as auxiliary electrode unless explicitly mentioned. All potentials in this work are reported versus Fc/Fc^+. The fully reduced species $\mathbf{Fe_5}^{2+}$ is air sensitive and thus needs to be isolated in an inert atmosphere. The fully oxidized

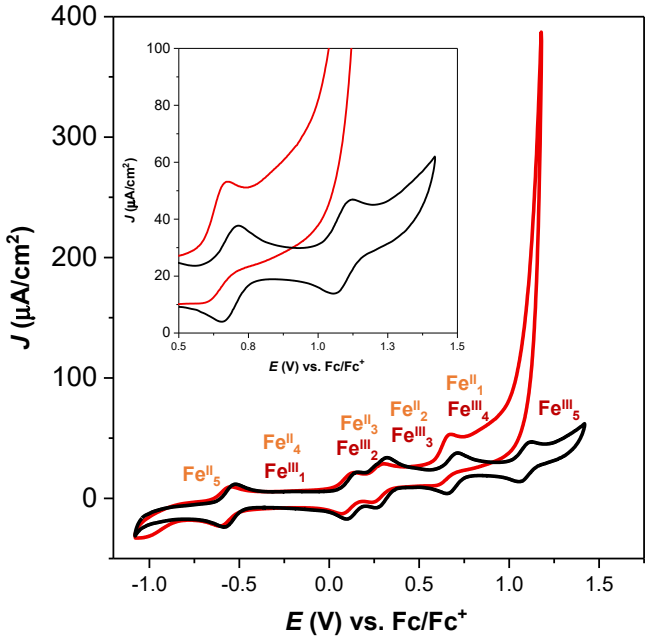

Figure 2. Electrochemical Characterization in MeCN of Fe_5^{3+}

Cyclic voltammetry experiments for Fe_5^{3+} 0.2 mM dissolved in a 0.1 M TEAP MeCN solution ($V_i = V_f = -0.24$ V; $V_{C1} = -1.08$ V; $V_{C2} = 1.42$ V) black trace, and in a 10:1 MeCN:H_2O volume ratio ($V_i = V_f = -0.24$ V, $V_{C1} = -1.08$ V; $V_{C2} = 1.19$ V) red trace (background subtracted) at a scan rate of 10 mV/s. Labels indicate the oxidation state zones of predominance as a function of potential. The inset shows an enlargement of the 0.6–1.4 V zone.

See also Tables S1 and S2 and Figure S4.

species, Fe_5^{7+}, displays a chemically reversible behavior during the CV timescale, but on bulk electrolysis timescales it is not stable and decomposes, indicating the high reactivity of such a high oxidation state species. All other Fe_5^{n+} species in intermediate oxidation states are stable and can be isolated as solids in an open air atmosphere that is in accordance with a previous report (Gouré et al., 2016).

The electronic structure of the six Fe_5^{n+} (n = 2–7) complexes at the different oxidation states has been unambiguously established based on EPR and magnetic measurements (Gouré et al., 2016). The six coordinated apical Fe(II) centers in Fe_5^{3+} have a low spin (LS) d^6 configuration, whereas two equatorial Fe(II) have a high spin (HS) d^6 and the third equatorial Fe(III) is a low spin d^5. On the other hand, for the highest oxidation state complex, Fe_5^{7+}, the apical Fe centers are LS, whereas the equatorial ones are HS.

Redox Properties in Aqueous MeCN

The Impact of [H_2O] in the Catalytic Activity

In water, the Fe_5^{3+} complex is not soluble, but it can be solubilized in mixtures of MeCN and H_2O. The latter is important since in the absence of water, the potential active species needed to enter into the water oxidation catalytic cycle cannot be formed. The electrochemical work reported here is carried out in mixtures of a MeCN solution containing 0.1 M tetraethyl ammonium perchlorate (TEAP) and water in a maximum 10:1 MeCN:H_2O volume ratio. This from now on will be referred in an abbreviated manner as 10:1 MeCN:H_2O.

In 10:1 MeCN:H_2O as solvent mixture the CV of Fe_5^{n+} is similar to the one reported in 0.1 M TEAP MeCN with a slight cathodic shift of roughly 40 mV for the wave associated with the $[Fe^{II}Fe^{III}_4]^{6+}/[Fe^{II}_2Fe^{III}_3]^{5+}$ couple as can be observed in Figure 2. Furthermore, a large electrocatalytic current starting at 0.85 V is observed that is assigned to the oxidation of water to dioxygen. This electrocatalytic wave was wrongly assigned to the catalytic activity of a molecular Fe_5^{n+} complex (Okamura et al., 2016). It was proposed based on DFT that, once the $[Fe^{III}_5]^{7+}$ species is reached, a solvent water molecule could coordinate in one of the equatorial iron centers forming $[Fe^{III}_5(H_2O)\ (\mu_3\text{-}O)\ (\mu\text{-bpp})_6]^{7+}$, with increasing coordination number from

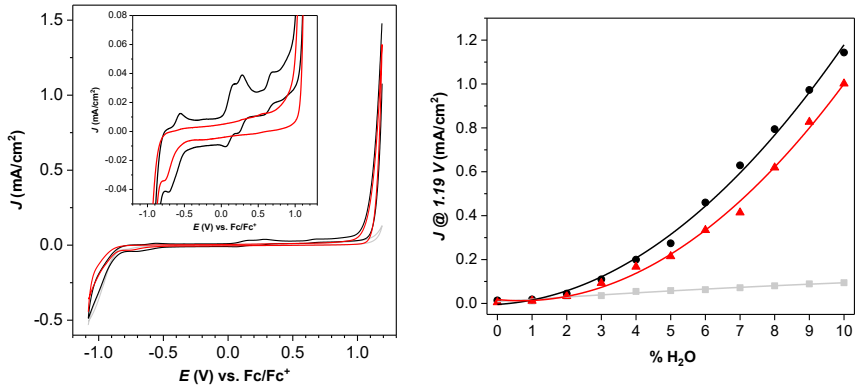

Figure 3. Electrochemical Analysis at Different Amounts of Water

Left, black trace, CV of the third cycle for $\mathbf{Fe_5}^{3+}$ 0.2 mM dissolved in a 10:1 MeCN:H_2O solution ($V_i = V_f = -1.08$ V; V_{C1} = 1.19 V) at a scan rate of 10 mV/s. Red trace, CV of the GC working electrode obtained in the previous experiment immersed in a clean electrolyte solution. Gray trace, CV of a bare GC electrode under the same conditions. Inset, enlargement in the zone of the non-catalytic waves of the complex. Right, plot of current density at 1.19 V under different MeCN:H_2O ratios obtained in the CV of: (1) black trace, after 2.5 cycles for a 0.2 mM $\mathbf{Fe_5}^{3+}$ solution with a GC electrode as WE at the previous conditions; (2) red trace, after the previous 2.5 cycles the GC electrode obtained is immersed in a clean electrolyte solution ($V_i = V_f$ = 0.92 V; V_{C1} = 1.19 V); (3) gray trace, blank for a bare GC electrode. See also Figures S5A and S5B.

CN_5 to CN_6. A series of oxidations and an additional water coordination to a neighboring Fe center was then proposed to occur so that a sufficiently reactive species would form an O-O bond that might finally release dioxygen. The transition state energy for the initial step, the coordination of water and the formation $[Fe^{III}_5(H_2O)\ (\mu_3\text{-}O)\ (\mu\text{-}bpp)_6]^{7+}$, is highly endergonic by 18.9 kcal/mol and is proposed to be the rate-determining step (rds) of this catalytic cycle (Liao et al., 2018). This is in agreement with the high stability of the $\mathbf{Fe_5}^{n+}$ structure and thus the large energy needed to disrupt it. On the other hand, it also points out that once a water molecule coordinates a metal center, the whole structure might collapse with the formation of multiple Fe complexes containing different ratios of aqua and bpp^- bonded ligands. If this disruption occurs in close proximity with a glassy carbon electrode the new species will generate FeOx as will be shown below.

Figure 3 left shows the third CV cycle of $\mathbf{Fe_5}^{3+}$ within the potential range of −1.08 to 1.19 V at a scan rate of 10 mV/s in 10:1 MeCN:H_2O solution (the first cycle is reported in Figure S5A). The waves associated with the $\mathbf{Fe_5}^{n+}$ molecular complex remain the same as in the first cycle (see Figure 2), whereas the catalytic current in the third cycle increases nearly five times from approximately 200 $\mu A/cm^2$ up to approximately 1.0 mA/cm^2 at 1.19 V. This unambiguously indicates the formation of new catalytically active species potentially adsorbed at the surface of the electrode. Indeed, transferring the glassy carbon electrode obtained after the CV into a clean electrolyte solution and scanning from 0.92 to 1.19 V shows a current density at 1.19 V that is close to 90% of the previous one. Furthermore, no redox waves associated with molecular $\mathbf{Fe_5}^{n+}$ complex can be observed when scanning within the −1.08 to 1.19 V potential range (see Figure 3 left). These two experiments point out that FeOx are the main species responsible for the electrocatalytic activity observed here, given its well-known catalytic behavior (Le Formal et al., 2015). Furthermore, X-ray absorption spectroscopy (XAS) was also carried out on glassy carbon plates, which gives additional support to the formation of FeOx adsorbed at the electrode surface as will be discussed later on.

A series of related experiments were also carried out by changing the relative concentration of H_2O from 1% to 10% in MeCN and are reported in the Figure S5B. In Figure 3 right a plot of the current density at 1.19 V versus the concentration of water is displayed for the initial $\mathbf{Fe_5}^{3+}$ solution and for the electrode obtained from this solution placed subsequently in a clean electrolyte solution. The very close values obtained here further point out that the $\mathbf{Fe_5}^{n+}$ species are a precursor for the generation of FeOx that is actually the active catalyst. The difference between the initial current density and the one obtained in a clean electrolyte solution can be due to ligand oxidation, the formation of transient active species generated during the decomposition process to FeOx, or from the partial solubilization of the FeOx from the electrode.

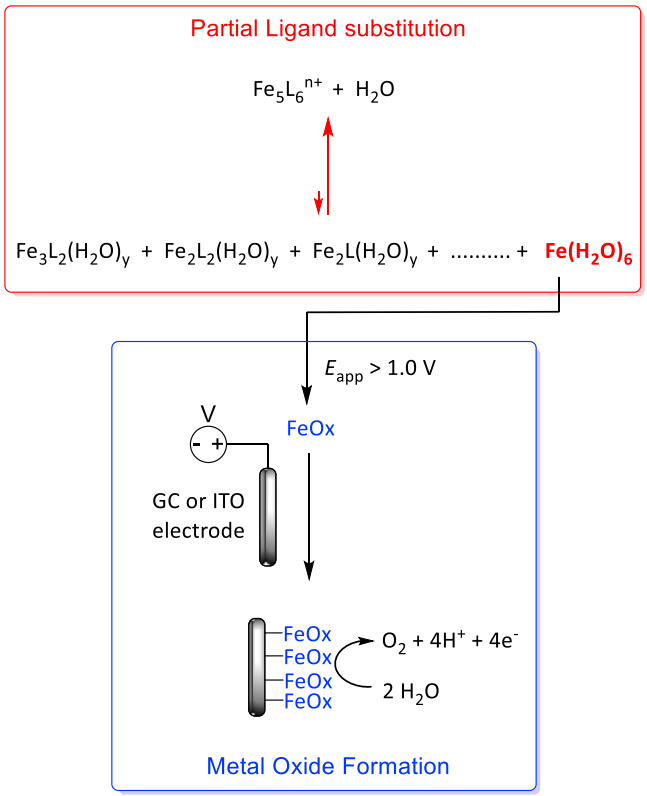

Figure 4. Scheme for the Formation of FeOx from Fe_5^{3+}

Potential non-isolated intermediate decomposition species formed from the Fe_5^{n+} complex toward the generation of free iron, $[Fe(H_2O)_6]^{n+}$, and the subsequent formation of the catalytically active species FeOx detected at the surface of an electrode.

As can be seen in Figure 3 right, the intensity of the wave at 1.19 V increases with the concentration of water thus clearly establishing a direct correlation between the H_2O concentration and the catalytic activity. This points out to the presence of a series of equilibria between the initial Fe_5^{n+} complex and FeOx as depicted in Figure 4. The larger the concentration of water, the larger is the equilibrium shift toward the aquated species, and thus a larger amount of FeOx will be deposited at the surface of the glassy carbon electrode. Furthermore, the increase in water concentration implies an increase in substrate concentration that can lead to a higher catalytic current.

The Influence of pH on the Stability of the Fe_5^{n+} Complex

The stability of Fe complexes is strongly dependent on pH as has been shown in a number of occasions for related ligands (Draksharapu et al., 2012; Hong et al., 2013). The main driving force for decomposition process is the lability of the bonded ligands that can be substituted by solvent water ligands. In acidic pH this substitution process will be further enhanced by the protonation of the bonded ligands that will be strongly dependent on pH. In this respect, the pK_a of pyridinium ion is 5.5 and that of pyrazole is 14.2. However, when the Hbpp is coordinated to a transition metal as in the case of $[Ru(trpy)(Hbpp)]^{2+}$ (where trpy is 2,2′:6′,2″-terpyridine), then the pK_a of the pyrazole moiety becomes more acidic with pK_a values in the range of 5–7 depending on the oxidation state of the metal (Sens et al., 2003). In basic pH, the anionic OH^- ligand will be responsible for the substitution process and subsequent generation of FeOx (Chen et al., 2013; Hong et al., 2013).

For water oxidation catalysis, the fact that every oxygen molecule evolved generates four protons implies that the local pH will also be strongly reduced in the double layer during water oxidation electrocatalysis. This will in turn strongly effect the stability of the complex leading to decomposition reactions at low local pHs. For this reason, it is extremely important to carry out water oxidation catalysis in the presence of a

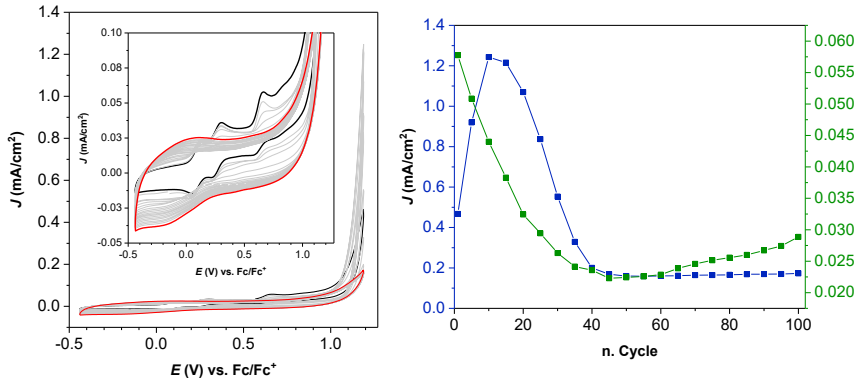

Figure 5. Stability Analysis and Formation of FeOx Film

Left, 100 repetitive CVs for $\mathbf{Fe_5}^{3+}$ 0.2 mM dissolved in 10:1 MeCN:H_2O ($V_i = V_f = -0.24$ V, $V_{C1} = -0.44$ V; $V_{C2} = 1.19$ V). Color code: black trace, first cycle; red trace, last cycle; gray traces, intermediate cycles displayed every five cycles. Right, blue trace, plot of the current density at 1.19 V as a function of CV cycles. Green trace, plot of $i_{p,a}$ of the $[Fe^{II}Fe^{III}_4]^{6+}$/$[Fe^{II}_2Fe^{III}_3]^{5+}$ redox wave as a function of CV cycles. See also Figures S8, S9, and S11.

buffer so that the pH can remain practically constant. This strong influence of pH into the electrocatalytic activity is clearly manifested by observing the current density in the CV at 1.19 V for $\mathbf{Fe_5}^{3+}$ in the presence and absence of buffer (see Figure S6 right). Indeed, in the absence of a buffer, the current density observed is 44% larger than the one in the presence of a non-coordinating borate buffer that clearly suggests the influence of the local pH on the equilibria proposed in Figure 4.

CV experiments were also carried out at different pH values, and it was found that from pH = 2–7, the behavior of the $\mathbf{Fe_5}^{n+}$ complex is basically the same (Okamura et al., 2016). However, below pH 2 the $\mathbf{Fe_5}^{3+}$ complex is not stable and decomposes to $[Fe^{II}(H_2O)_6]^{2+}$ and free ligand as is the case of related complexes reported in the literature (Draksharapu et al., 2012; Hong et al., 2013). Furthermore, no electrocatalytic activity is observed at pH values below 2. (see Figure S7 for further details).

The Formation of FeOx Films at the Surface of the GC Electrode

The nature of the FeOx deposited at the surface of the GC electrode was evaluated by means of electrochemical, spectroscopic, and microscopy techniques. Figure 5 left shows the results of 100 repetitive CVs scans from −0.44 to 1.19 V for a 0.2 mM solution of $\mathbf{Fe_5}^{3+}$ in a 10:1 MeCN:H_2O solution using a GC disk as a working electrode (GC). As it can be observed after the 100th cycle, the CV becomes nearly featureless with an increased double layer capacitance indicating that the initial electrode has lost its conductivity. A simply eye inspection of the electrode shows the formation of a film at the surface. Placing this electrode into a clean solution containing a ferrocene solution 0.2 mM shows that the anodic III/II wave has lost 93.3% (see Figure S8) of its area with regard to a pristine electrode in exactly the same conditions, confirming the isolating nature of the oxide deposited at the electrode.

The SEM image of this electrode does not show any boundary or particle shapes, but rather a homogeneous surface with similar morphology as the GC electrode, and thus we attribute this to the formation of a film. The nature of this film was further evaluated based on energy-dispersive X-ray (EDX) spectroscopy, scanning electron microscopy (SEM), and X-ray photoelectron spectroscopy (XPS) displayed in the Supplemental Information (Figures S9 and S11 top, respectively). XANES (X-ray absorption near edge structure) and EXAFS (extended X-ray absorption fine structure analysis) were also carried out on the $\mathbf{Fe_5}^{n+}$ complex before (Figures S19-S21, Table S3) and after bulk catalysis (Figure 6) in a glassy carbon plate following exactly the same protocol used for the CV with the GC disk electrode. The XANES and EXAFS spectra shown in Figure 6 unequivocally show the spectral features of FeOx (Kuzmin and Chaboy, 2014; Tangwatanakul et al., 2017) at the electrode after the 100th cycle, thus discarding the potential surface absorption of the molecular $\mathbf{Fe_5}^{n+}$ species. As observed by the red arrows in Figure 6B, a prominent increase in the amplitudes of the EXAFS peaks at apparent distances ∼1.5 and 2.5 Å are indeed observed in agreement with the EXAFS spectral features of Fe_2O_3 (shown in cyan).

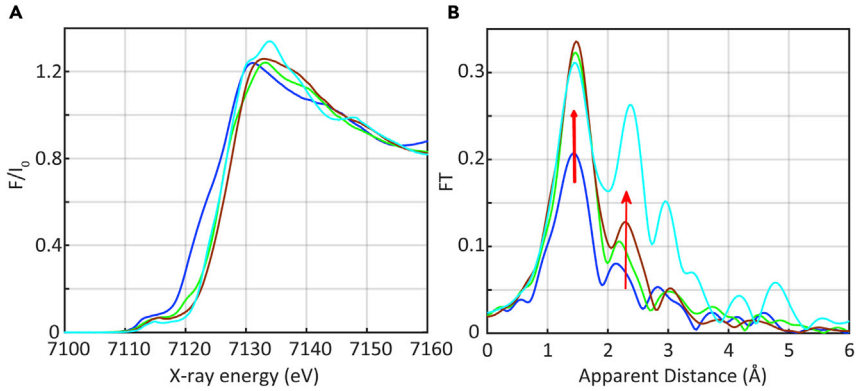

Figure 6. X-ray Absorption Spectroscopy of the FeOx Electroactive Species

(A) Normalized Fe K-edge XANES of: (1) the $\mathbf{Fe_5}^{3+}$ complex in a frozen mixture of 10:1 MeCN:H_2O (blue); (2) the frozen solution obtained after bulk electrolysis of $\mathbf{Fe_5}^{3+}$ at an applied potential of 1.42 V for 30 min (green; see main text and Supplemental Information for further experimental details); (3) glassy carbon plate (used as a working electrode) obtained after 100 successive CV experiments carried out in the ranges of −0.44 to 1.19 V of 0.2 mM solution of the $\mathbf{Fe_5}^{3+}$ complex in a mixture of 10:1 MeCN:H_2O (brown); (4) Fe_2O_3 powder (cyan). (B) Experimental Fourier transforms of k-weighted Fe EXAFS of the samples described in the left using the same color code. The red arrows indicate the main peaks associated with Fe_2O_3. See also Table S3 and Figures S19–S21.

A closer inspection at the repetitive CV experiment provides additional insight into the progressive formation of the FeOx film. Figure 5 right shows a plot of the current density obtained at 1.19 V versus $i_{p,a}$ of the $[Fe^{II}Fe^{III}_4]^{6+}/[Fe^{II}_2Fe^{III}_3]^{5+}$ redox wave preceding the electrocatalytic current. During the first ten cycles, the electrocatalytic current at 1.19 V increases its intensity, whereas the $i_{p,a}$ of the $[Fe^{II}Fe^{III}_4]^{6+}/[Fe^{II}_2Fe^{III}_3]^{5+}$ wave decreases. This implies that the catalytic activity increases initially as active FeOx is being formed and deposited at the GC electrode. At the same time and owing to the formation of non-conductive FeOx (potentially due to a thicker layer or different morphology), the available conductive surface area decreases and thus the intensity of the molecular $\mathbf{Fe_5}^{n+}$ waves decreases as well. The next 20 cycles show a decrease of both currents owing to the non-conductive nature of the film generated at the electrode. From 50 to 100 cycles, small amounts of isolating FeOx are further deposited, which generates a large increase of the capacitance at the electrode.

The Formation of FeOx Nanoparticles at the Surface of the GC Electrode

The performance of the $\mathbf{Fe_5}^{3+}$ complex was evaluated by multiple consecutive cycle voltammetric experiments under a different range of potentials. Figure 7 left shows 50 repetitive cyclic voltammetry experiments carried out in exactly the same conditions as the previous one but after changing the potential range from −1.08 to 1.19 V to fully reduce the initial complex all the way to the $Fe^{II}_5{}^{2+}$ species. Figure 7 right also shows the current density plot obtained at 1.19 V versus $i_{p,a}$ of the $[Fe^{II}Fe^{III}_4]^{6+}/[Fe^{II}_2Fe^{III}_3]^{5+}$ redox wave. As the number of cycles proceed, the catalytic intensity at 1.19 V increases owing to the increasing amount of FeOx adsorbed at the GC electrode until it reaches a plateau due to the saturation of the surface. On the other hand, the intensity of the molecular $\mathbf{Fe_5}^{n+}$ species waves decrease owing to a decrease of the concentration of the double layer caused by the formation of FeOx. As can be seen in the Figure 7, the FeOx deposited at the electrode is conductive. The formation of nanoparticles can be observed with SEM (see Figure S10) with an approximate diameter of about 40 nm.

The conductivity of the material also enables us to observe the formation of other electroactive species growing at the double layer (see cathodic waves at −0.25 and 0.75 V in Figure 7 left). This suggests that the initial $\mathbf{Fe_5}^{n+}$ complex decomposes to other molecular species as indicated in Figure 4, before forming FeOx, which finally ends up being adsorbed at the surface of the electrode.

Potentiostatic Generation of FeOx

Potentiostatic experiments were carried out using a glassy carbon rod (GCrod) or indium tin oxide (ITO) as a working electrode as shown in the Supplemental Information (see Figures S12, S14, and S17).

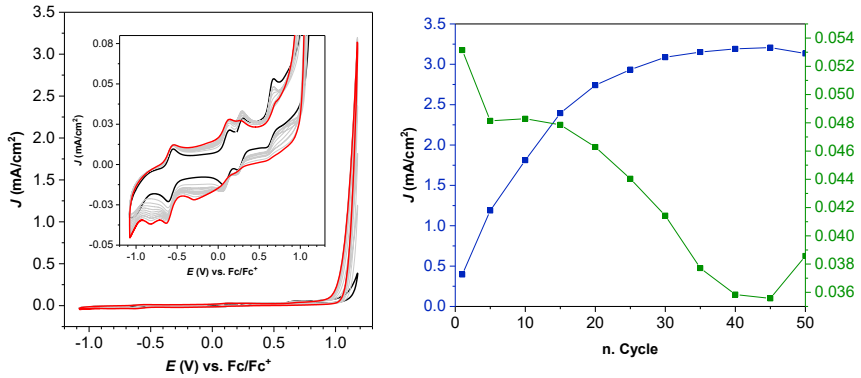

Figure 7. Stability Analysis and Formation of FeOx Active Nanoparticles

Left, 50 repetitive CVs for $\mathbf{Fe_5}^{3+}$ 0.2 mM dissolved in 10:1 MeCN:H_2O ($V_i = V_f = -0.24$ V, $V_{C1} = -1.08$ V; $V_{C2} = 1.19$ V). Color code: black trace, first scan; red trace, last scan; gray traces, intermediate cycles displayed every five cycles. Right, blue trace, plot of the current density at 1.19 V as a function of CV cycles. Green trace, plot of $i_{p,a}$ of the $[Fe^{II}Fe^{III}_4]^{6+}$/$[Fe^{II}_2Fe^{III}_3]^{5+}$ redox wave as a function of CV cycles. See also Figures S10 and S11.

A controled potential electrolysis (CPE) was performed with a GCrod as working electrode with 6.5 mL of a 0.2 mM (1.3 μmol) solution of $\mathbf{Fe_5}^{3+}$ and was carried out for 1 h at E_{app} = 1.19 V. During this time 1.05 C was passed together with the formation of 2.5 μmol of O_2 that accounts for 90 of faradaic efficiency (FE) (see Figures S12 and S13). Oxygen detection obtained through Clark electrode.

Potentiostatic experiments using ITO electrodes (S = 2 cm^2) as working electrodes are shown in the Supplemental Information (Figures S14 and S17). Same conditions previously described, 6.5 mL of a 0.2 mM (1.3 μmol) solution of $\mathbf{Fe_5}^{3+}$ was applied. One CPE was carried out for 1 h at E_{app} = 1.42 V. During this time 7.5 C (77 μmol of electrons/4 = 19.4 μmol of O_2) was obtained, which corresponds to a TN = 14.9 assuming a 100% FE (calculated for comparison purposes; see Figure S14). After the bulk electrolysis the ITO electrode was placed in a clean electrolyte solution and it showed the same activity as in the presence of the $\mathbf{Fe_5}^{3+}$ solution, demonstrating again that the water oxidation activity is due to the formation of FeOx at the surface of the electrode (Figure S15 left). Furthermore, a CV using a GC disk as working electrode was carried out for the $\mathbf{Fe_5}^{3+}$ solution obtained after the bulk electrolysis and showed no molecular species present indicating that the whole solution is transformed to FeOx (see Figures S15 and S16). An additional bulk electrolysis was carried out at E_{app} = 1.19 V (Figure S17) under the same conditions as in the previous case using an ITO electrode (S = 2 cm^2), yielded 1 C (10.2 μmol of electrons/4 = 2.5 μmol of O_2), which corresponds to a TN = 1.9 assuming a 100% faradaic efficiency. The CV of the solution after the CPE shows that a significant amount of the initial complex together with other waves associated with potential decompositions of the initial $\mathbf{Fe_5}^{3+}$ complex is still present (Figure S18 right). This implies that the initial complex has only been partially decomposed to FeOx and that this process is taking place slowly and in parallel to the electrocatalytic formation of O_2 by the adsorbed FeOx.

DISCUSSION

The compact structure of the $\mathbf{Fe_5}^{3+}$ complex is a highly stable structural arrangement and thus constitutes a thermodynamic sink in the sense that all intermediate species generated from the reaction of bpp^- and Fe(II) can break and form new Fe-N bonds until they end up trapped in $\mathbf{Fe_5}^{3+}$. This implies that bond formation and breaking acts as an automatic healing process that leads to the final $\mathbf{Fe_5}^{3+}$ complex. A similar type of phenomenon has been described in supramolecular chemistry for the generation of macrocycles and cages based on other transition metals (Cook et al., 2013). This large stability is also displayed by related tetradentate linear ligands with Fe and other first row transition metal complexes such as Mn that generate virtually identical structures (Kabata-pendias and Mukherjee, 2007). The large degree of stability is also manifested in the large energy value (18.9 kcal/mol) calculated that is required to coordinate an additional water molecule to one of the equatorial Fe center, changing its first coordination sphere from CN_5 to CN_6.

These pentanuclear complexes are very stable from a thermodynamic perspective, but they also are highly labile owing to their high spin electronic configurations. Thus, although these complexes are stable in

MeCN solution, they readily decompose in the presence of coordinating solvents such as water, where the latter competes for the first coordination sphere. This decomposition phenomenon involves the disruption of the whole complex leading to a structure crumbling effect that finally generates the $[M(H_2O)_6]^{2+/3+}$ and the free ligand as has been reported for the $\mathbf{Mn_5}^{3+}$ case. The $\mathbf{Fe_5}^{3+}$ complex is slightly more stable than its Mn analog and can tolerate concentrations up to 10:1 MeCN:H_2O at low oxidation states. However, the stability of the complex is reduced in its high oxidation state species even in MeCN. Although the $[\mathbf{Fe^{II}Fe^{III}_4}]^{6+}$ decomposes completely in about 1 h, the $[\mathbf{Fe^{III}_5}]^{7+}$ decomposes much faster and has not been isolated (Gouré et al., 2016). Electrochemically, the $[\mathbf{Fe^{II}Fe^{III}_4}]^{6+}$ species are not stable in a 10:1 MeCN:H_2O solution as ascertained by CV leading to the aquated species (Figure 4). Additionally, increasing the applied potential to the zone of predominance of the $[\mathbf{Fe^{III}_5}]^{7+}$ species leads to the formation of FeOx concomitant with the generation of a large electrocatalytic water oxidation current. The fact that the foot of the electrocatalytic current is found at a 150 mV lower potential than the foot of the $[\mathbf{Fe^{III}_5}]^{7+}$/$[\mathbf{Fe^{II}Fe^{III}_4}]^{6+}$ couple suggests that both the $[\mathbf{Fe^{II}Fe^{III}_4}]^{6+}$ and the $[\mathbf{Fe^{III}_5}]^{7+}$ might be responsible for the aquation of the $\mathbf{Fe_5}^{n+}$ species that leads to the formation of FeOx adsorbed at the electrode. Given the large stability of the $\mathbf{Fe_5}^{n+}$ structure, once a water adds to the first coordination sphere of an equatorial Fe center, the whole structure immediately crumbles giving rise to a large number of potential species as outlined in Figure 4. This view is also in agreement with the increased catalytic activity obtained upon increasing the H_2O concentration, which shifts the equilibria to the right as shown in Figure 3. These molecular high-oxidation-state species generated at high potentials from the dismantling of the $\mathbf{Fe_5}^{n+}$ structure could potentially behave as water oxidation catalysts. However, in the present case, given the large activity associated with FeOx, the activity of the resulting decomposed species is small if not active at all, as evidenced by CV experiments in clean electrolyte solutions.

All these experiments suggest the presence of a very delicate equilibrium between the $[\mathbf{Fe^{II}Fe^{III}_4}]^{6+}$ and the $[\mathbf{Fe^{III}_5}]^{7+}$ species, and their aquated counterparts as proposed in Figure 4. An additional evidence of this delicate equilibrium is exemplified by the experiments carried out in the presence of triflic acid that completely suppresses catalysis. Furthermore, the experiments carried out at different pHs suggest the local pH close to the electrode can reach pH values as low as 1, in experiments carried out in the absence of a buffer, for instance, in a 10:1 MeCN:H_2O solvent. The low pH conditions could further help in the aquation of the $\mathbf{Fe_5}^{3+}$ complex and thus in the generation of FeOx.

An additional interesting point that also emerges from this work is how the nature of the FeO_x formed at the surfaces of the electrode (conductive versus isolating; films versus nanoparticles), is strongly dependent on the potential range used to generate it. Furthermore, it is also striking to see the high activity of this FeOx adsorbed at the surface of the electrode that reaches current densities in the range of 3 mA/cm^2 at pH 7.

In this regard, the high activity of the FeOx could lead to a misinterpretation of the results if the working electrodes are not properly evaluated in clean electrolyte solutions, since only very small amounts of the initial molecular complex are needed to be transformed into highly active FeOx. Thus, in the hypothetical case that the stability of the complex in solutions after a bulk electrolysis experiment was checked, for instance, by UV-vis, MS, or DLS spectroscopy, it would appear as if the initial catalyst was intact as the initial concentration would remain practically the same.

Several main conclusions can be inferred from the present work. In the first place, the auxiliary ligands used in WOCs with transition metals should contain oxidatively robust ligands given the high redox potentials of this reaction. Therefore, ligands containing benzyl pyridyl groups will be easily oxidized as has been shown in many cases (Radaram et al., 2011; Sander et al., 2015; Wang et al., 2016). Thus, they should not be used in their ligand framework. Second, special attention should be given to the stability of first row transition metals in water given the high lability of the M-L bond in this solvent (Helm and Merbach, 2006). The aqua substitution will foster the formation of oxides adsorbed at the surface of the electrode. Finally, the fact that the water oxidation reaction generates four protons per oxygen molecule implies that a buffer should always be used to avoid ligand decoordination and oxide formation.

Limitation of the Study

No limitation of the study can be declared.

Resource Availability

Lead Contact

Further information and requests should be directed to the Lead Contact, Antoni Llobet (allobet@iciq.cat).

Materials Availability

No new reagents were synthetized. There are no restrictions to the availability of chemicals.

Data and Code Availability

Crystallographic information for $[Fe^{II}_2Fe^{III}_3]^{5+}$ with CCDC number 1963878 is available at https://www.ccdc.cam.ac.uk/.

METHODS

All methods can be found in the accompanying Transparent Methods supplemental file.

SUPPLEMENTAL INFORMATION

Supplemental Information can be found online at https://doi.org/10.1016/j.isci.2020.101378.

ACKNOWLEDGMENTS

Support from MINECO, FEDER, and AGAUR is gratefully acknowledged through grants CTQ2016-80058-R, CTQ2015-73028-EXP, SEV 2013-0319, ENE2016-82025-REDT, CTQ2016-81923-REDC, and 2017-SGR-1631. D.M. acknowledges funding from the Severo Ochoa (SEV-2016-0686) Excellence Program from IMDEA Nanociencia. XAS experiments were performed at the CLAESS beamline at ALBA Synchrotron under proposal No. 20170913 and 2017032110.

AUTHOR CONTRIBUTIONS

A.L. conceived the idea of the project. P.P. performed the synthesis, characterization, and electrochemical experiments. M.G.-S. assisted with the electrochemical experiments. D.M. performed the XAS experiments. All authors contributed to the design of experiments, analysis of the results, and preparation of the manuscript.

DECLARATION OF INTERESTS

The authors declare no competing interests.

Received: June 8, 2020
Revised: July 2, 2020
Accepted: July 14, 2020
Published: August 21, 2020

REFERENCES

Bao, X., Leng, J.-D., Meng, Z.-S., Lin, Z.-J., Tong, M.-L., Nihei, M., and Oshio, H. (2010). Tuning the spin states of two apical iron(II) ions in the Trigonal-bipyramidal $[\{Fe^{II}(\mu\text{-bpt})_3\}_2Fe^{II}_3(\mu_3\text{-O})]^{2+}$ cations through the choice of anions. Chem. Eur. J. *16*, 6169–6174.

Berardi, S., Drouet, S., Francàs, L., Gimbert-Suriñach, C., Guttentag, M., Richmond, C., Stoll, T., and Llobet, A. (2014). Molecular artificial photosynthesis. Chem. Soc. Rev. *43*, 7501–7519.

Blakemore, J.D., Crabtree, R.H., and Brudvig, G.W. (2015). Molecular catalysts for water oxidation. Chem. Rev. *115*, 12974–13005.

Chen, G., Chen, L., Ng, S.-M., Man, W.-L., and Lau, T.-C. (2013). Chemical and visible-light-driven water oxidation by iron complexes at pH 7–9: evidence for dual-active intermediates in iron-catalyzed water oxidation. Angew. Chem. Int. Ed. *52*, 1789–1791.

Cook, T.R., Zheng, Y.R., and Stang, P.J. (2013). Metal–Organic frameworks and self-assembled supramolecular coordination complexes: comparing and contrasting the design, synthesis, and functionality of Metal–Organic materials. Chem. Rev. *113*, 734–777.

Croce, R., and van Amerongen, H. (2014). Natural strategies for photosynthetic light harvesting. Nat. Chem. Biol. *10*, 492–501.

Draksharapu, A., Li, Q., Logtenberg, H., Van den Berg, T.A., Meetsma, A., Killeen, J.S., Feringa, B.L., Hage, R., Roelfes, G., and Browne, W.R. (2012). Ligand exchange and spin state equilibria of Fe^{II}(N4Py) and related complexes in aqueous media. Inorg. Chem. *51*, 900–913.

Ellis, W.C., McDaniel, N.D., Bernhard, S., and Collins, T.J. (2010). Fast water oxidation using iron. J. Am. Chem. Soc. *32*, 163–170.

Folkman, S.J., Soriano-Lopez, J., Galá-Mascarós, J.R., and Finke, R.G. (2018). Electrochemically driven water-oxidation catalysis beginning with six exemplary cobalt polyoxometalates: is it molecular, homogeneous catalysis or electrode-bound, heterogeneous CoOx catalysis? J. Am. Chem. Soc. *140*, 12040–12055.

Garrido-Barros, P., Gimbert-Suriñach, C., Matheu, R., Sala, X., and Llobet, A. (2017). How to make an efficient and robust

molecular catalyst for water oxidation. Chem. Soc. Rev. *46*, 6088–6098.

Godwin, I., Rovetta, A., Lyons, M., and Coleman, J. (2018). Electrochemical water oxidation: the next five years. Curr. Opin. Electrochem *7*, 31–35.

Gouré, E., Gerey, B., Clémancey, M., Pécaut, J., Molton, F., Latour, J.M., Blondin, G., and Collomb, M.N. (2016). Intramolecular electron transfers Thwart bistability in a pentanuclear iron complex. Inorg. Chem. *55*, 9178–9186.

Grätzel, M. (1981). Artificial photosynthesis: water cleavage into hydrogen and oxygen by visible light. Acc. Chem. Res. *14*, 376–384.

Guan, X., Chowdhury, F.A., Wang, Y., Pant, N., Vanka, S., Trudeau, M.L., Guo, L., Vayssieres, L., and Mi, Z. (2018). Making of an industry-friendly artificial photosynthesis device. ACS Energy Lett. *3*, 2230–2231.

Helm, L., and Merbach, A.E. (2006). Inorganic and bioinorganic solvent exchange mechanisms. Chem. Rev. *105*, 1923–1960.

Hoffert, W.A., Mock, M.T., Appel, A.M., and Yang, J.Y. (2013). Incorporation of hydrogen-bonding functionalities into the second coordination sphere of iron-based water-oxidation catalysts. Eur. J. Inorg. Chem. *22-23*, 3846–3857.

Hong, D., Mandal, S., Yamada, Y., Lee, Y.M., Nam, W., Llobet, A., and Fukuzumi, S. (2013). Water oxidation catalysis with nonheme iron complexes under acidic and basic conditions: homogeneous or heterogeneous? Inorg. Chem. *52*, 9522–9531.

Kabata-pendias, A., and Mukherjee, A.B. (2007). Trace Elements from Soil to Human. (Springer).

Kaeffer, N., Morozan, A., Fize, J., Martinez, E., Guetaz, L., and Artero, V. (2016). The dark side of molecular catalysis: Diimine–Dioxime cobalt complexes are not the actual hydrogen evolution electrocatalyst in acidic aqueous solutions. ACS Catal. *6*, 3727–3737.

Keidel, A., Lopez, I., Staffa, J., Kuhlmann, U., Bozoglian, F., Gimbert-Surinach, C., Benet-Buchholz, J., Hildebrandt, P., and Llobet, A. (2017). Electrochemical and resonance Raman spectroscopic studies of water-oxidizing ruthenium terpyridyl-bipyridyl complexes. ChemSusChem *10*, 551–561.

Kuzmin, A., and Chaboy, J. (2014). EXAFS and XANES analysis of oxides at the nanoscale. IUCrJ *1*, 571–589.

Le Formal, F., Pastor, E., Tilley, S.D., Mesa, C.A., Pendlebury, S.R., Grätzel, M., and Durrant, J.R. (2015). Rate law analysis of water oxidation on a Hematite surface. J. Am. Chem. Soc. *137*, 6629–6637.

Lewis, N.S., and Nocera, D.G. (2006). Powering the planet: chemical challenges in solar energy utilization. Proc. Nat. Acad. Sci. U S A *103*, 15729–15735.

Lewis, N.S., and Nocera, D.G. (2007). Correction for Lewis and Nocera, Powering the planet: chemical challenges in solar energy utilization. Proc. Nat. Acad. Sci. U S A *104*, 20142.

Lewis, N.S. (2016). Research opportunities to advance solar energy utilization. Science *351*, 353–361.

Liao, R.Z., Masaoka, S., and ad Siegbahn, P.E.M. (2018). On the metal oxidation states for the O-O bond formation in the water oxidation catalyzed by a pentanuclear Iron complex. ACS Catal. *8*, 11671–11678.

Llobet, A., and Meyer, F. (2011). Water oxidation in the context of the energy challenge: tailored transition-metal catalysts for oxygen-oxygen bond formation. Angew. Chem. Int. Ed. *50*, 30–33.

Matheu, R., Ertem, M.Z., Benet-Buchholz, J., Coronado, E., Batista, V.S., Sala, X., and Llobet, A. (2015). Intramolecular proton transfer boosts water oxidation catalyzed by a Ru complex. J. Am. Chem. Soc. *137*, 10786–10795.

Matheu, R., Garrido-Barros, P., Gil-Sepulcre, M., Ertem, M.Z., Sala, X., Gimbert-Suriñach, C., and Llobet, A. (2019a). The development of molecular water oxidation catalysts. Nat. Rev. Chem. *3*, 331–341.

Matheu, R., Ertem, Z.M., Gimbert-Suriñach, C., Sala, X., and Llobet, A. (2019b). Seven coordinated molecular ruthenium-water oxidation catalysts: a coordination chemistry journey. Chem. Rev. *119*, 3453–3471.

McCrory, C.C.L., Jung, S., Ferrer, I.M., Chatman, S.M., Peters, J.C., and Jaramillo, T.F. (2015). Benchmarking hydrogen evolving reaction and oxygen evolving reaction electrocatalysts for solar water splitting devices. J. Am. Chem. Soc. *137*, 4347–4357.

McEvoy, J.P., and Brudvig, G.W. (2006). Water-splitting chemistry of photosystem II. Chem. Rev. *106*, 4455–4483.

Nelson, N., and Ben-Shem, A. (2004). The complex architecture of oxygenic photosynthesis. Nat. Rev. Mol. Cell. Biol. *5*, 971–982.

Nocera, D.G. (2017). Solar fuels and solar chemicals industry. Acc. Chem. Res. *50*, 616–619.

Okamura, M., Kondo, M., Kuga, R., Kurashige, Y., Yanai, T., Hayami, S., Praneeth, V.K.K., Yoshida, M., Yoneda, K., Kawata, S., and Masaoka, S. (2016). A pentanuclear iron catalyst designed for water oxidation. Nature *530*, 465–468.

Pattanayak, S., Chowdhury, D.R., Garai, B., Singh, K.K., Paul, A., Dhar, B.B., and Gupta, S.S. (2017). Electrochemical formation of FeV(O) and mechanism of its reaction with water during O—O bond formation. Chem. Eur. J. *23*, 3414–3424.

Radaram, B., Ivie, J., Singh, W.M., Grudzient, R.M., Reibenspies, J.H., Webster, C.E., and Zhao, X. (2011). Water oxidation by mononuclear ruthenium complexes with TPA-based ligands. Inorg. Chem. *50*, 10564–10571.

Roger, I., Shipman, M.A., and Symes, M.D. (2017). Earth-abundant catalysts for electrochemical and photoelectrochemical water splitting. Nat. Rev. Chem. *1*, 301–313.

Romain, S., Rich, J., Sens, C., Stoll, T., Benet-Buchholz, J., Llobet, A., Rodriguez, M., Romero, I., Clerac, R., Mathoniere, C., et al. (2011). Multireversible redox processes in Pentanuclear Bis(Triple-Helical) Manganese omplexes featuring an oxo-centered triangular $\{Mn^{II}_2Mn^{III}(\mu_3\text{-}O)\}^{5+}$ or $\{Mn^{II}Mn^{III}_2(\mu_3\text{-}O)\}^{6+}$ core wrapped by two $\{Mn^{II}_2(bpp)_3\}^{-}$. Inorg. Chem. *50*, 8427–8436.

Sala, X., Maji, S., Bofill, R., Garcia-Anton, J., Escriche, L., and Llobet, A. (2014). Molecular water oxidation mechanisms followed by transition metals: state of the art. Acc. Chem. Res. *47*, 504–516.

Sander, A.C., Schober, A., Dechert, S., and Meyer, F. (2015). A pyrazolate-bridged Bis(pentadentate) ligand and its dinuclear ruthenium complex. Eur. J. Inorg. Chem. *26*, 4348–4353.

Sens, C., Rodríguez, M., Romero, I., Llobet, A., Parella, T., and Benet-Buchholz, J. (2003). Synthesis, structure and acid-base and redox properties of a family of new Ru(II) isomeric complexes containing the trpy and the dinucleating Hbpp ligands. Inorg. Chem. *42*, 8385–8394.

Smith, R.D., Prévot, M.S., Fagan, R.D., Zhang, Z., Sedach, P.A., Siu, M.K., Trudel, S., and Berlinguette, C.P. (2013). Photochemical route for accessing amorphous metal oxide materials for water oxidation catalysis. Science *340*, 60–63.

Sreerama, S.G., and Pal, S. (2004). A triiron complex containing the carboxylate-free $\{Fe_3(\mu_3\text{-}O)\}^{7+}$ core and distorted pentagonal-bipyramidal metal centres. Eur. J. Inorg. Chem. *3*, 4718–4723.

Tangwatanakul, W., Sirisathitkul, C., Limphirat, W., and Yimnirun, R. (2017). Synchrotron X-ray absorption of iron oxide (Fe2O3) nanoparticles: effects of reagent concentration and sonication in co-precipitation synthesis. Chin. J. Phys. *55*, 845.

Wang, J.-W., Sahoo, P., and Lu, T.-B. (2016). Reinvestigation of water oxidation catalyzed by a dinuclear cobalt polypyridine complex: identification of CoOx as a real heterogeneous catalyst. ACS Catal. *6*, 5062–5068.

iScience, Volume *23*

Supplemental Information

Analysis of the Active Species Responsible for Water Oxidation Using a Pentanuclear Fe Complex

Primavera Pelosin, Marcos Gil-Sepulcre, Pablo Garrido-Barros, Dooshaye Moonshiram, Jordi Benet-Buchholz, Carolina Gimbert-Suriñach, and Antoni Llobet

Supplemental Information

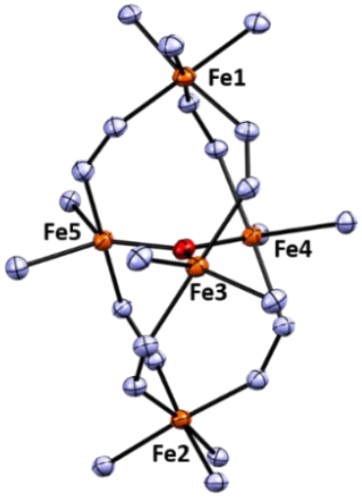

Figure S1. Schematic ORTEP drawing (ellipsoids 50 %) of $[Fe^{II}_2Fe^{III}_3]^{5+}$, related to Figure 1. The Fe centers are represented as orange ellipsoids and are numbered from 1 to 5. The further structure of bpp^- ligand, H atoms, counter ions and solvent molecules are not represented for simplicity reasons. Color code: red = O; orange = Fe; blue = N.

Table S1. Fe – O bond distances in Å for $[Fe^{II}_4Fe^{III}]^{3+}$ and $[Fe^{II}_2Fe^{III}_3]^{5+}$, extracted from X-ray structures. Related to Figures 1 and S1.

Entry	Atoms	$[Fe^{II}_4Fe^{III}]^{3+}$	$[Fe^{II}_2Fe^{III}_3]^{5+}$
1	Fe_1 - O	3.85	3.84
2	Fe_2 - O	3.85	3.87
3	Fe_3 - O	1.93	1.80
4	Fe_4 - O	1.93	1.93
5	Fe_5 - O	1.99	1.94

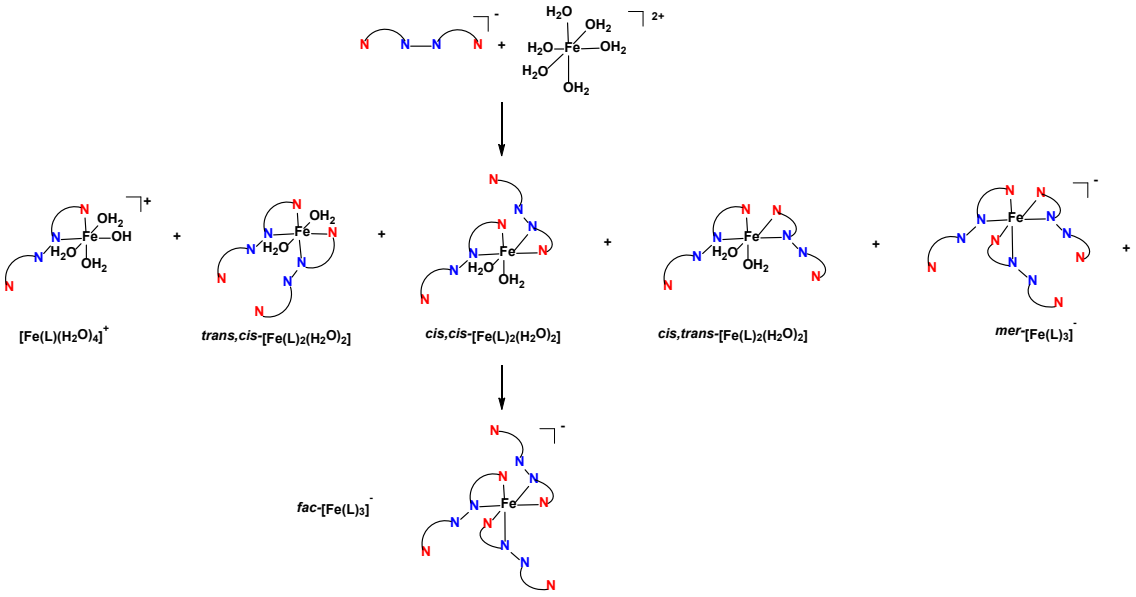

Figure S2. **Fe_5^{n+} formation (thermodynamic path), related to Figure 1**. Potential non-isolated Fe complexes that can be formed at the Initial stages of the reaction of Fe(II) and L^- (bpp^-) to form **Fe_5^{3+}**. The arcs connected with N represent the bpp^- ligand. Red N represent pyridyl groups whereas the blue ones represent pyrazolyl groups.

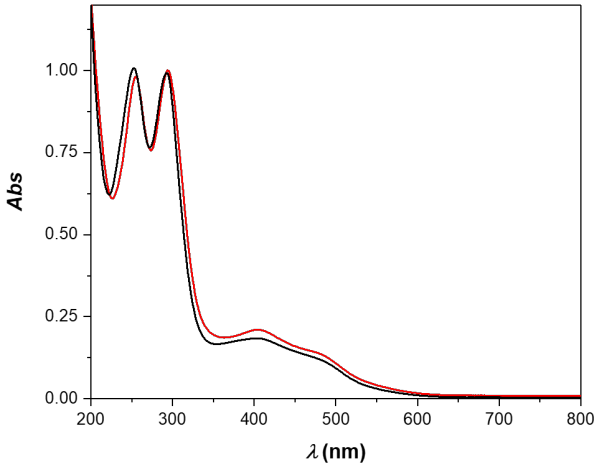

Figure S3. UV-Vis spectra of the reaction mixture and the isolated crystals, related to Figures 1 and S2. UV-Vis absorption spectrum in a MeOH:H_2O (10:3) solution of: a) black trace, a 0.07 mM of an isolated and crystallized sample of [**Fe$_5$**$(BF_4)_3$]·$7H_2O$ and b) a diluted solution directly from the synthesis. A 0.2 cm path length quartz cuvette was used. For the **Fe$_5$**$^{3+}$ 0.140 mg of [**Fe$_5$**$(BF_4)_3$]·$7H_2O$ (MW, 2009.15, 0.07 μmols) dissolved in MeOH:H_2O (10:3) solution up to a total volume of 1.0 mL. This generates a 0.07 mM solution of [**Fe$_5$**$(BF_4)_3$]. For the reaction mixture, the same procedure as in the synthesis was flollowed. A sample of $FeSO_4$·$7H_2O$ (84 mg, 0.3 mmol; 0.05 M) + Hbpp (80 mg, 0.36 mmol; 0.06 M) + NaOH (14 mg, 0.36 mmol; 0.06 M) was dissolved with 10:3 MeOH:H_2O up to a total volume of 6 mL. Then the solution was stirred at RT for a few minutes. An aliquot of the resulting solution was diluted to reach a formal concentration of bpp$^-$ of 0.42 mM.

Table S2. $E_{1/2}$ values for all the redox processes of Fe_5^{3+} in MeCN and 10:1 MeCN:H_2O containing TEAP (0.1 M) as supporting electrolyte. Related to Figure 2.

Entry	Redox Couple	$E_{1/2}$ (E (V) vs Fc/Fc^+)	
		CH_3CN	10:1 MeCN:H_2O
1	$[Fe^{II}_4Fe^{III}]^{3+}/[Fe^{II}_5]^{2+}$	-0.55	-0.57
2	$[Fe^{II}_3Fe^{III}_2]^{4+}/[Fe^{II}_4Fe^{III}]^{3+}$	0.13	0.11
3	$[Fe^{II}_2Fe^{III}_3]^{5+}/[Fe^{II}_3Fe^{III}_2]^{4+}$	0.30	0.29
4	$[Fe^{II}Fe^{III}_4]^{6+}/[Fe^{II}_2Fe^{III}_3]^{5+}$	0.68	0.64
5	$[Fe^{III}_5]^{7+}/[Fe^{II}Fe^{III}_4]^{6+}$	1.08	1.19 ($E_{p,a}$)

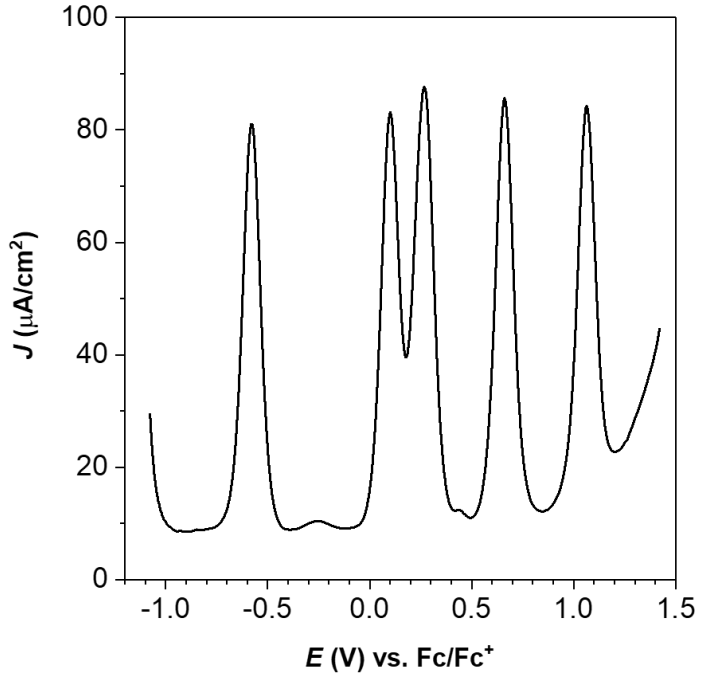

Figure S4. **Differential Pulse Voltammetry, related to Figure 2.** 0.2 mM solution of $\mathbf{Fe_5}^{3+}$ in MeCN (V_i -1.08 V; V_f = 1.42 V). Amplitude= 50 mV, step height= 4 mV, pulse width= 0.05 s, pulse period= 0.2 s and sampling width= 0.0167 s.

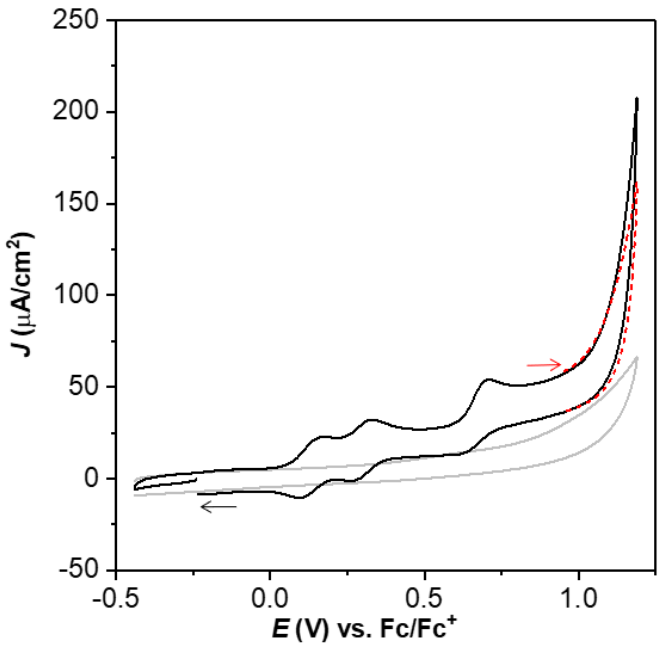

Figure S5A. First cycle, related to Figure 3. Solid black trace, CV of the first cycle for $\mathbf{Fe_5}^{3+}$ 0.2 mM in MeCN containing 10% of H_2O at a scan rate of 10 mV/s. The black arrow indicates the scan direction. Dash red trace, base line subtracted CV of the GC working electrodes obtained in the previous experiment, immersed in a clean electrolyte solution of MeCN containing 10% of H_2O at a scan rate of 10 mV/s. The red arrow indicates scan direction. Gray trace, CV of a bare GC electrode in the same conditions.

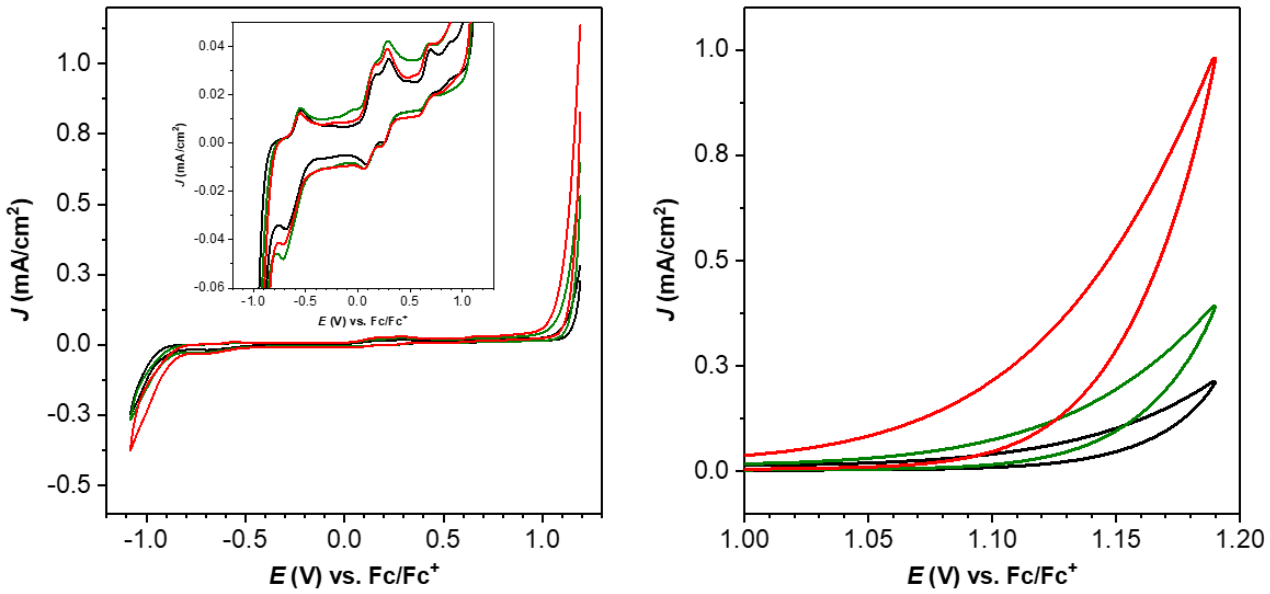

Figure S5B. CVs at different concentration of water, related to Figure 3. Left, CV of the 2.5th for **Fe$_5$**$^{3+}$ 0.2 mM in MeCN containing 10% (red trace), 7 % (green trace) and 5 % (black trace) of H_2O at a scan rate of 10 mV/s ($V_i = V_f$ = -1.08 V; V_{C1} = 1.19 V). *Inset*, enlargement on the wave of the complex. Right, CV of the GC working electrodes obtained in the previously mentioned experiments (left) under the same conditions immersed in a clean electrolyte solution ($V_i = V_f$ = 0.92 V; V_{C1} = 1.19 V).

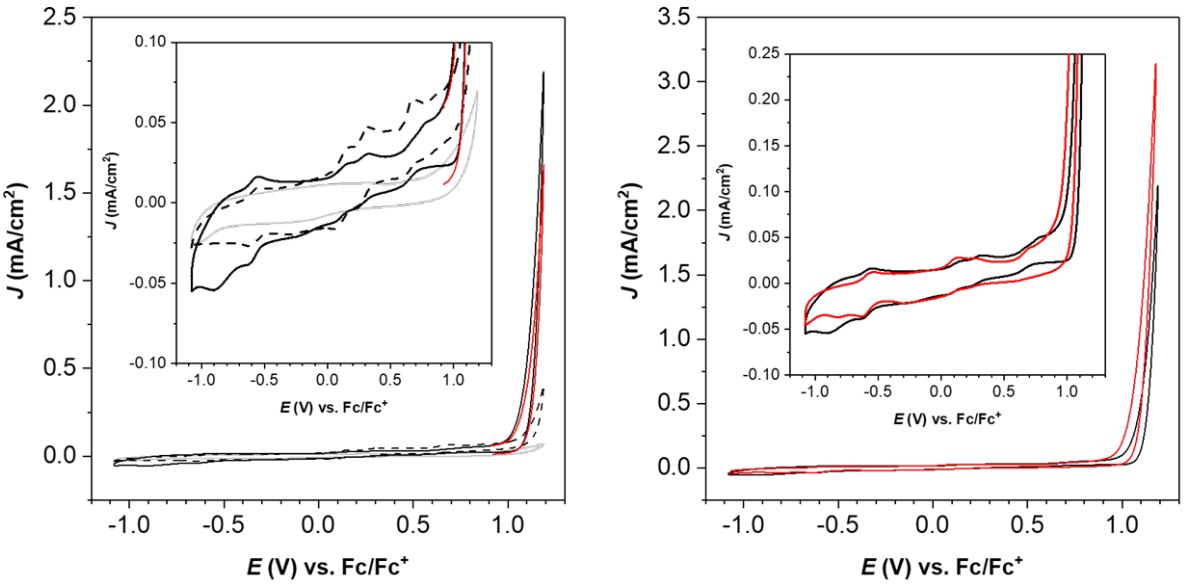

Figure S6. CV cycles in a buffered solution, related to Figure 3. Left, black trace, CV of the 50th cycle for **Fe$_5$**$^{3+}$ 0.2 mM dissolved in a 10:1 MeCN:H_2O solution (added H_2O contains 0.01 M borate buffer, pH 7.8) at a scan rate of 10 mV/s (V_i = V_f = -1.08 V; V_{C1} = 1.19 V). Black dashed trace, CV of the 1st cycle. Red trace, CV of the GC working electrode obtained in the previous experiment immersed in a clean electrolyte solution. Gray trace, CV of a bare GC electrode under the same conditions. *Inset*, enlargement on the wave of the complex. Right, black trace, CV of the 50th cycle for **Fe$_5$**$^{3+}$ 0.2 mM dissolved in a 10:1 MeCN:H_2O solution (added H_2O contains 0.01 M borate buffer, pH 7.8) at a scan rate of 10 mV/s (V_i = V_f = -1.08 V; V_{C1} = 1.19 V). Red trace, CV of the 50th cycle for **Fe$_5$**$^{3+}$ under the same conditions but adding pure H_2O

.

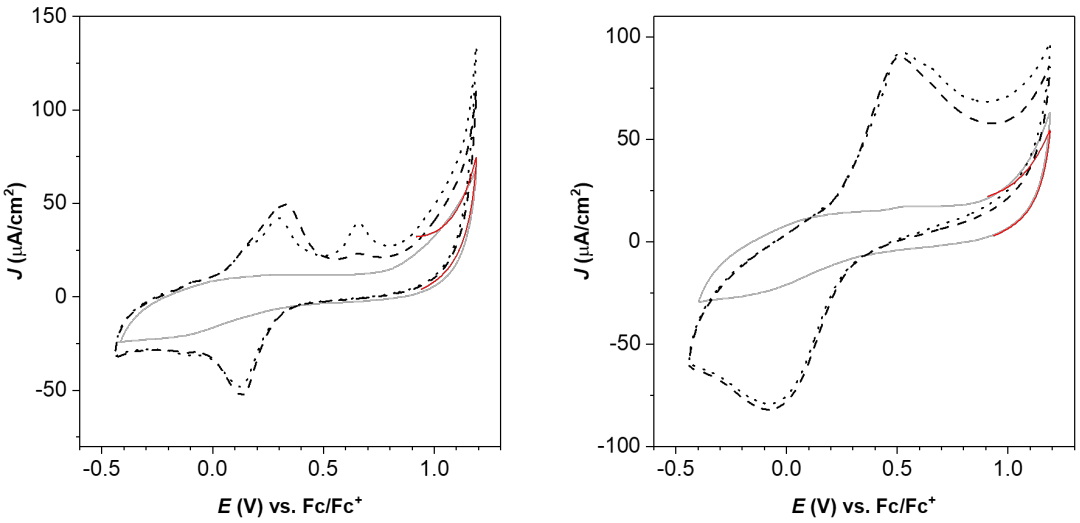

Figure S7. CV cycles at pH 1 and 0.5, related to Figure 3. CVs for $\mathbf{Fe_5}^{3+}$ 0.2 mM dissolved in a 10:1 MeCN:H_2O solutions, performed with 0.1 M triflic acid solution pH 1 (left) and 0.3 M triflic acid solution pH 0.5 (right), at a scan rate of 10 mV/s. *Color code:* black dotted trace, CV of the first cycle; black dashed trace, CV of the second cycle; red trace, CV of the GC working electrode obtained in the previous experiment immersed in a clean electrolyte solution. Gray trace, bare GC electrode. For black dotted, black dashed and grey traces, $V_i = V_f = -0.44$ V; $V_{C1} = 1.19$ V. For the red trace, $V_i = V_f = 0.92$ V; $V_c = 1.19$ V.

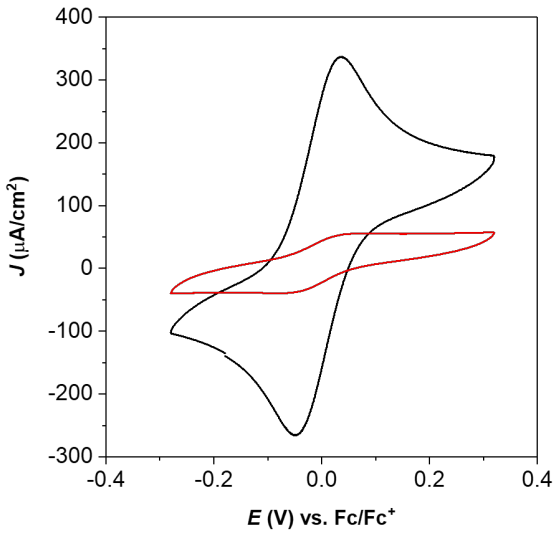

Figure S8. Conductivity test with ferrocene, related to Figure 5. CVs of a 0.2 mM ferrocene solution in 10:1 MeCN:H_2O before (black trace) and after (red trace) cycling the GC electrode (V_i = V_f = -0.44 V, V_{C1} = -0.44 V; V_{C2} = 1.19 V) 100 times in a solution 0.2 mM of $\mathbf{Fe_5}^{3+}$ in a 10:1 MeCN:H_2O.

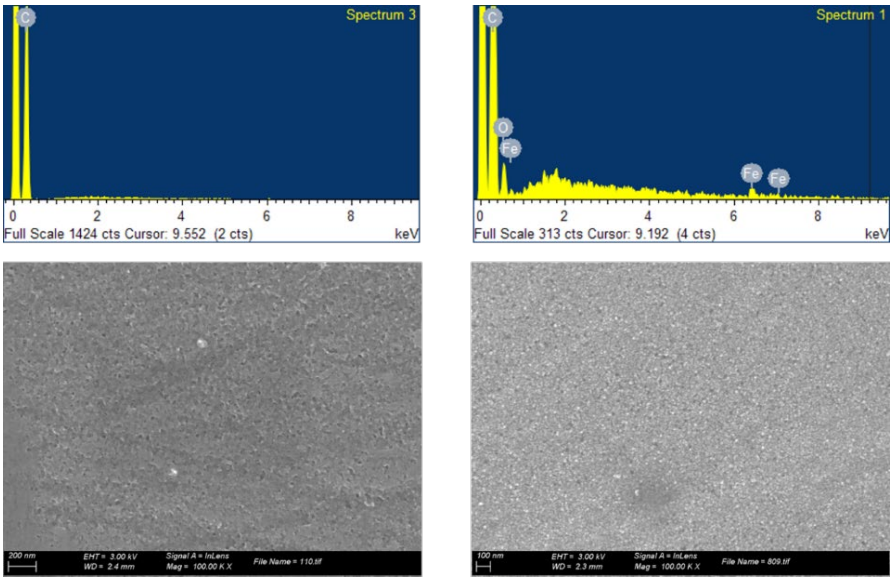

Figure S9. EDX and SEM analysis, related to Figure 5. EDX analysis (top) and SEM pictures (bottom) of the GC_{rod} (d= 3 mm) surface after cycling 100 times ($V_i = V_f = -0.44$; $V_C = 1.19$ V) in a complex-free 10:1 MeCN:H_2O solution (left) and in a solution of $\mathbf{Fe_5}^{3+}$ 0.2 mM (right) in 10:1 MeCN:H_2O, at scan rate of 10 mV/s.

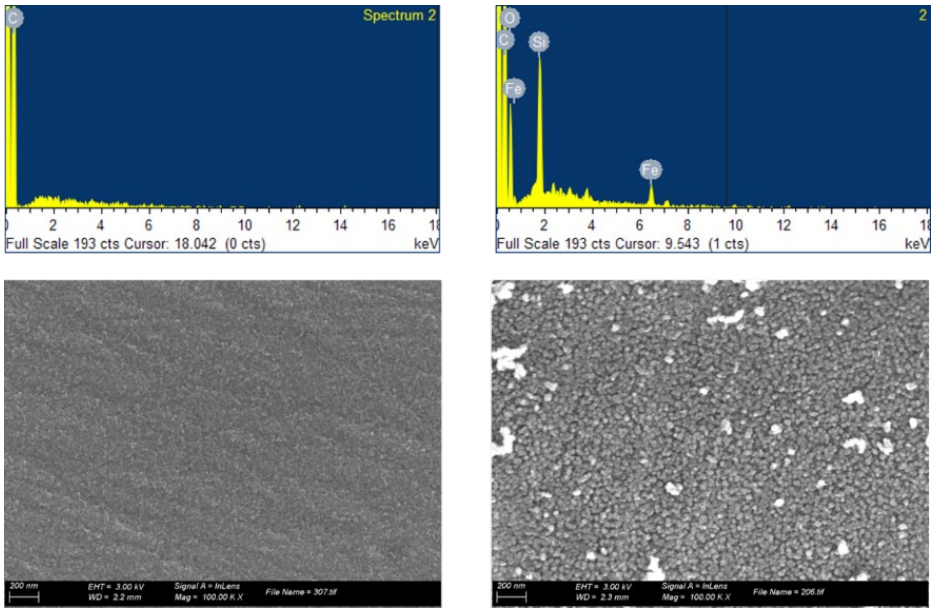

Figure S10. EDX and SEM analysis, related to Figure 7. EDX analysis (top) and SEM pictures (bottom) of the GC_{rod} (d= 3 mm) surface after cycling 50 times ($V_i = V_f = -1.08$; $V_C = 1.19$ V) in a complex-free 10:1 MeCN:H_2O solution (left) and in a solution of $\mathbf{Fe_S}^{3+}$ 0.2 mM (right) in 10:1 MeCN:H_2O, at scan rate of 10 mV/s.

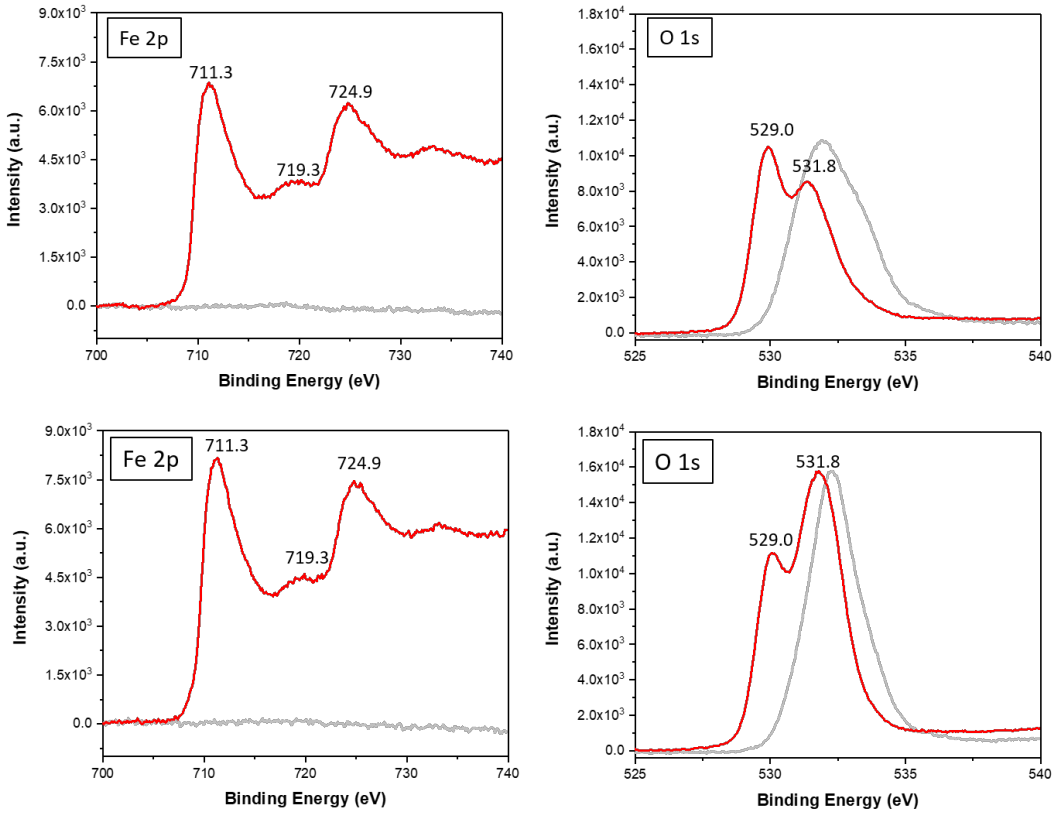

Figure S11. XPS analysis, related to Figure 5 and 7. Fe 2p (left) and O 1s (right) XPS spectra of the GC_{rod} (d= 3 mm) surface after cycling in a solution of $\mathbf{Fe_5}^{3+}$ 0.2 mM (red trace) in 10:1 MeCN:H_2O and in a complex-free 10:1 MeCN:H_2O solution (gray trace), at scan rate of 10 mV/s. Top, 100 CV cycles, $V_i = V_f = -0.44$; $V_C = 1.19$ V; Bottom, 50 CV cycles, $V_i = V_f = -1.08$; $V_C = 1.19$ V. Energies have been calibrated according to the C 1s band of graphite at 284.2 eV.

Table S3. EXAFS Fits parameters, Related to Figures 6 and S19-S20.

Sample	Fit	Peak	Shell,N	R, Å	E_0	ss.^{2} (10^{-3})	R-factor	Reduced Chi-square
Fe_5^{3+} powder	1	1	Fe-N/O, 5.4	2.03	-7.8	9.2	0.0028	236
	2	I,II	Fe-N/O, 5.4 Fe-C, 8	2.03 2.96	-7.9	9.3 52.2	0.0057	204
	3	all	Fe-N/O,5.4 Fe-C, 8 Fe-C, 21	2.04 2.93 3.09	-5.5	9.1 17.1 7.6	0.0005	27
	4	all	**Fe-N/O, 5.4** **Fe-C, 8** **Fe-C, 21** **Fe-C, 36**	**2.04** **2.98** **3.14** **3.56**	**-6.0**	**9.3** **16.6** **34.2** **10.3**	**0.0082**	**299**
Fe_5^{3+} dissolved in pure CH_3CN	5	1	Fe-N/O, 5.4	2.02	-7.6	11.7	0.0104	223
	6	I,II	Fe-N/O, 5.4 Fe-C, 8	2.02 2.99	-7.1	11.7 50.7	0.0224	187
	7	all	Fe-N/O, 5.4 Fe-C, 8 Fe-C, 21	2.04 2.95 3.12	-4.8	11.2 14.5 6.1	0.0083	117
	8	all	**Fe-N/O, 5.4** **Fe-C, 8** **Fe-C, 21** **Fe-C, 36**	**2.05** **2.98** **3.15** **3.54**	**-4.3**	**11.6** **11.2** **16.4** **13.9**	**0.0132**	**124**
Fe_5^{3+} dissolved in CH_3CN: H_2O (10:1)	9	1	Fe-N/O, 5.4	2.01	-8.7	11.6	0.0091	63
	10	I,II	Fe-N/O, 5.4 Fe-C, 8	2.02 3.03	-7.3	11.7 46.2	0.0196	52
	11	all	Fe-N/O, 5.4 Fe-C, 8 Fe-C, 21	2.03 2.97 3.14	-5.1	11.0 16.1 8.8	0.0089	40
	12	all	**Fe-N/O, 5.4** **Fe-C, 8** **Fe-C, 21** **Fe-C, 36**	**2.03** **2.98** **3.19** **3.50**	**-5.0**	**11.4** **10.3** **16.8** **10.6**	**0.0095**	**29**

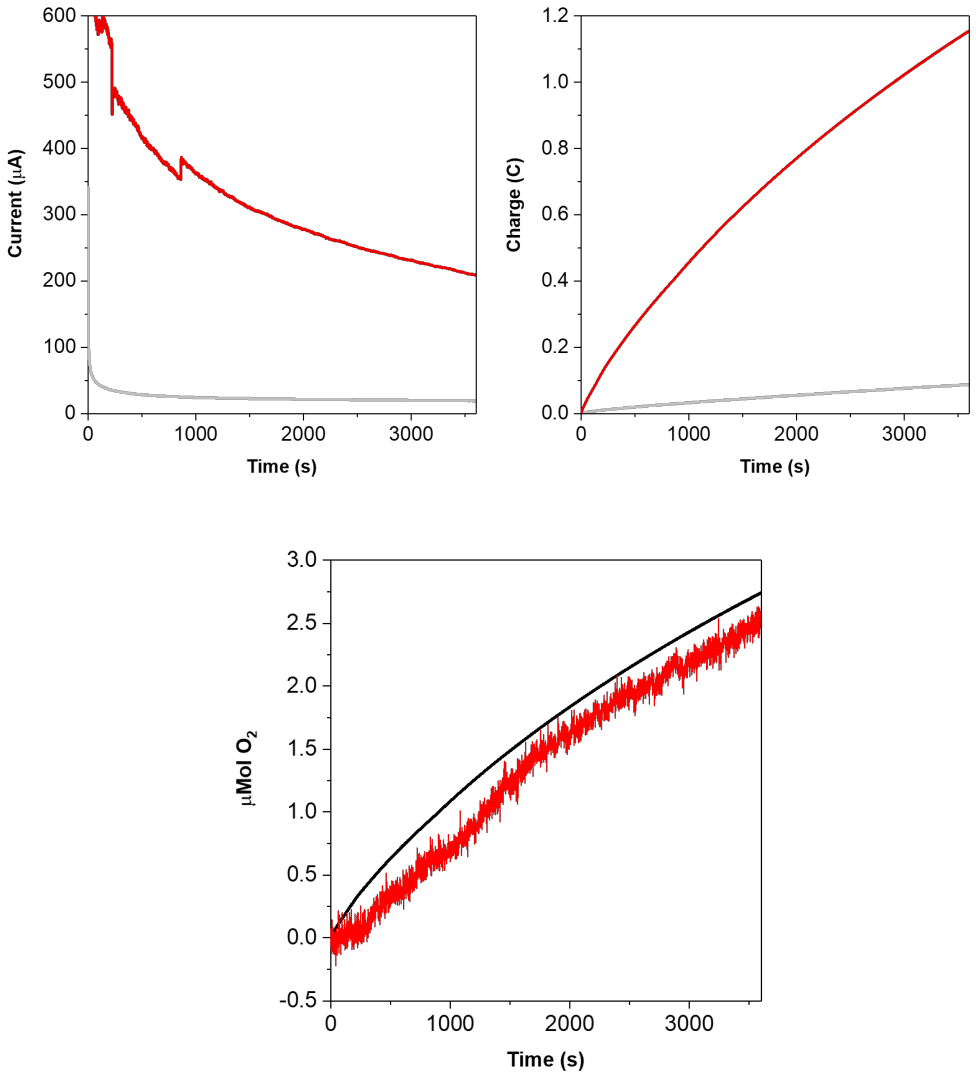

Figure S12. CPE at 1.19 V with GC_{rod} as WE, and O_2 detection, related to Figure 4. Current (left) and charge (right) profiles generated during the CPE experiment at E_{app} = 1.19 V performed under N_2 atmosphere with **Fe_5^{3+}** 0.2 mM in 6.5 mL 10:1 MeCN:H_2O solution (red trace) and with a complex-free 10:1 MeCN:H_2O solution (gray trace) during 3600 seconds. Charge, 1.05 C (blank subtracted) -> 10.8 μmols of e^-, TN = 2.1 (assuming 100 % of Faradaic efficiency; 1.9 with 90%). Electrodes: GC_{rod} (2 cm immersed in the solution) (WE), Pt mesh (CE), Ag/Ag^+ (RE).

Blank subtracted oxygen evolution (bottom) detected by a Clark electrode for the above CPE up to 3600 s. The ratio between the theoretical oxygen evolved (black line) calculated from the generated charge and the experimental oxygen evolved (red line), gives a Faradaic efficiency of 90 %.

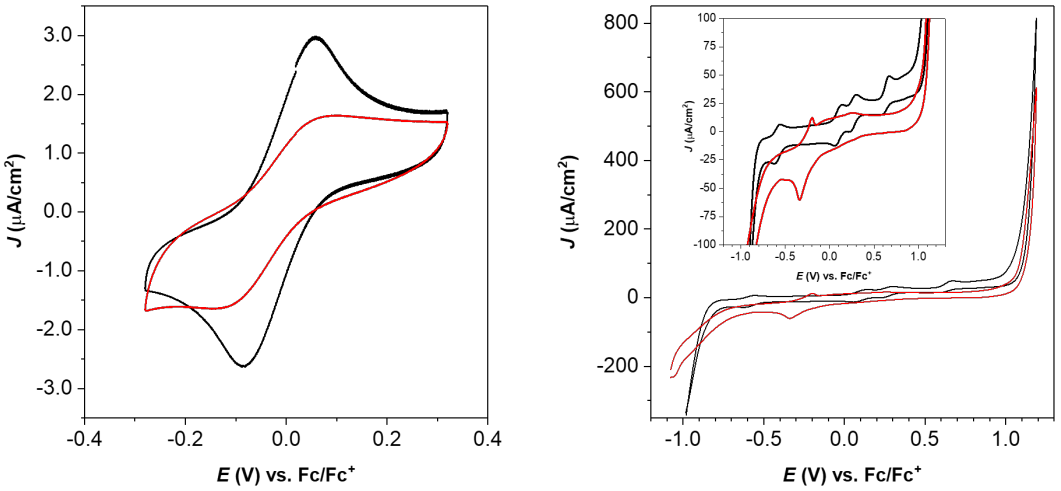

Figure S13. Electrochemical analysis of the electrode and of the solution after the CPE at 1.19 V, related to Figures 4 and S12. Left, CVs of GC_{rod} used in the previous experiment (CPE in Figure S12) in a 0.2 mM ferrocene solution in 10:1 MeCN:H_2O before (black trace) and after (red trace) the CPE experiment at a scan rate of 10 mV/s. Right, CVs of $\mathbf{Fe_5}^{3+}$ 0.2 mM in a 10:1 MeCN:H_2O solution using a GC disk as WE, before (black trace) and after (red trace) the CPE experiment (Figure S12), at a scan rate of 100 mV/s. Electrodes: GC disk (WE), Pt (CE), Ag/Ag^+ (RE).

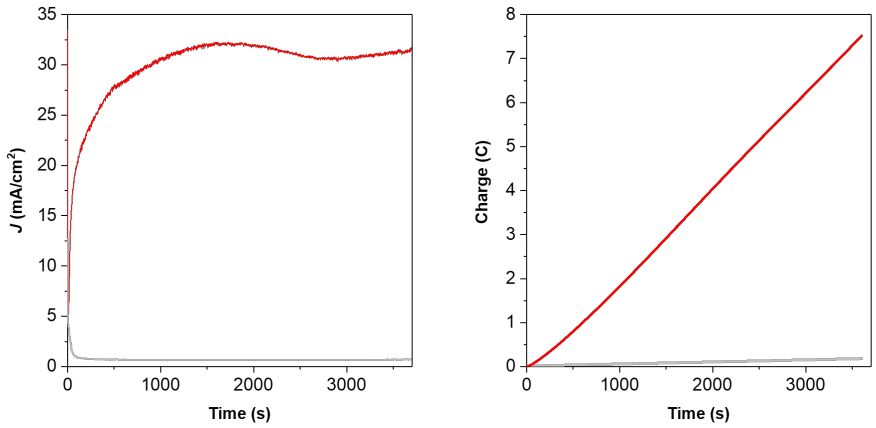

Figure S14. CPE at 1.42 V with ITO as WE, related to Figure 4. Current (left) and charge (right) profiles generated during the CPE experiment at E_{app} = 1.42 V performed under N_2 atmosphere with **Fe$_5$**$^{3+}$ 0.2 mM in 6.5 mL 10:1 MeCN:H_2O solution (red trace) and with a complex-free 10:1 MeCN:H_2O solution (gray trace) during 3600 s. Charge, 7.5 C -> 77 µmols of e^-, TON = 14.9 (assuming 100 % of Faradaic efficiency). Electrodes: ITO electrode (S = 2 cm^2) (WE), Pt mesh (CE), Ag/Ag$^+$ (RE).

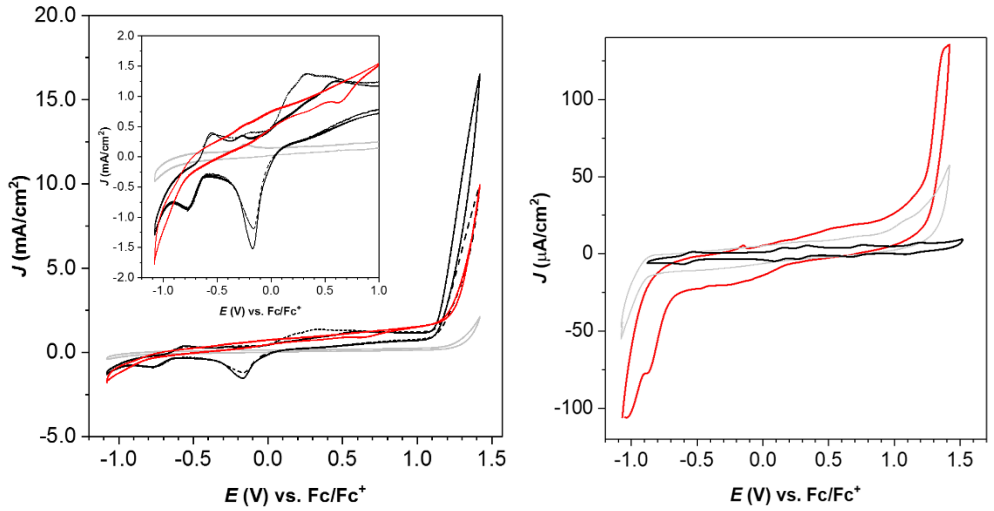

Figure S15. Electrochemical analysis of the electrode and of the solution after the CPE at 1.42 V, referred to Figures 4 and S14. Left, black dashed trace, first CV cycle of $\mathbf{Fe_5}^{3+}$ 0.2 mM dissolved in 10:1 MeCN:H_2O before CPE experiment (Figure S14), at a scan rate of 100 mV/s ($V_i = V_f$ = -1.08 V; V_{C1} = 1.42 V). Black solid trace, second CV cycle. Red trace, CV of the ITO working electrode obtained after the previously mentioned CPE experiment immersed now in a clean electrolyte solution. Gray trace, CV of a bare ITO electrode under the same conditions. ITO electrode (S = 2 cm^2) (WE), Pt mesh (CE), Ag/Ag^+ (RE). Right, red trace, CV of $\mathbf{Fe_5}^{3+}$ 0.2 mM dissolved in 10:1 MeCN:H_2O after CPE experiment (Figure S14), at a scan rate of 100 mV/s ($V_i = V_f$ = -1.08 V; V_{C1} = 1.42 V). Black trace, CV of $\mathbf{Fe_5}^{3+}$ 0.2 mM dissolved in MeCN. Gray trace, CV of a bare GC electrode under the same conditions. GC (WE), Pt mesh (CE), Ag/Ag^+ (RE).

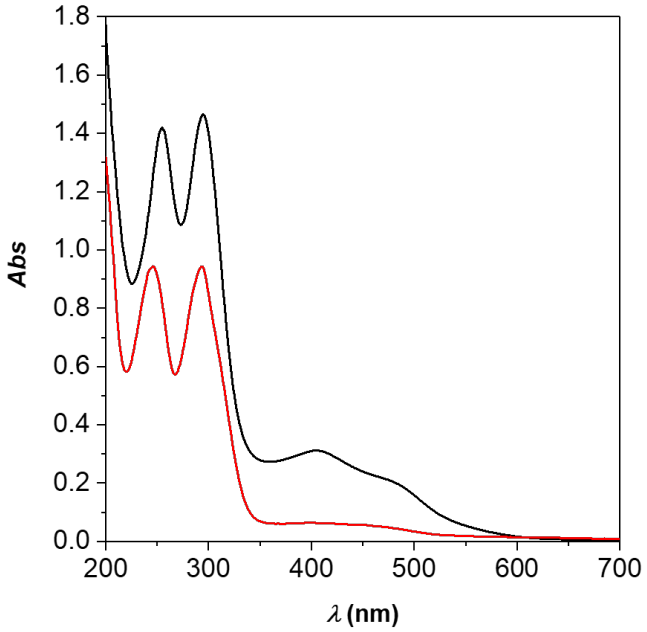

Figure S16. UV-Vis analysis of the solution after the CPE at 1.42 V, referred to Figures 4 and S14. Comparison of UV-Vis absorption spectra of a 0.2 mM solution of $\mathbf{Fe_5}^{3+}$ in 10:1 MeCN:H_2O containing TEAP 0.1 M as supporting electrolyte before (black trace) and after (red trace) the CPE at E_{app}= 1.42 V.

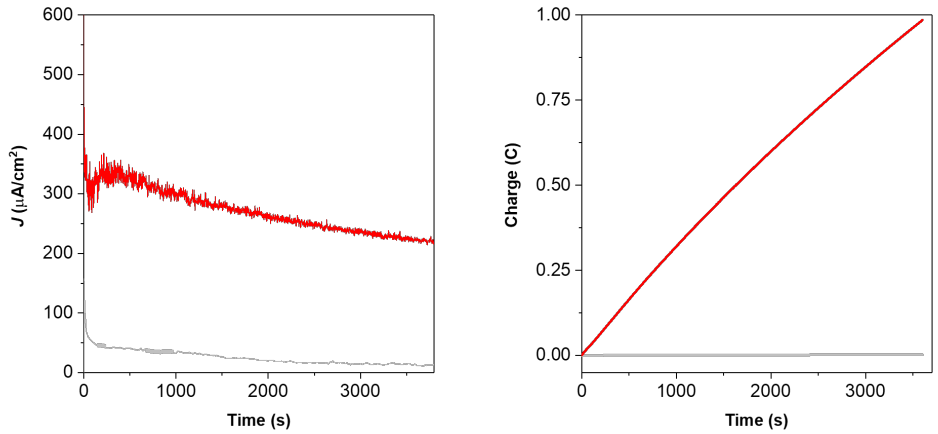

Figure S17. CPE at 1.19 V with ITO as WE, related to Figure 4. Current (left) and charge (right) profiles generated during the CPE experiment at E_{app}=1.19 V performed under N_2 atmosphere with **Fe$_5$**$^{3+}$ 0.2 mM in 6.5 mL 10:1 MeCN:H_2O solution (red trace) and with a complex-free 10:1 MeCN:H_2O solution (gray trace) during 3600 seconds. Charge, 0.98 C -> 10.2 µmols of e^-, TN = 1.9 (assuming 100 % of Faradaic efficiency). Electrodes: ITO electrode (S = 2 cm^2) (WE), Pt mesh (CE), Ag/Ag$^+$ (RE).

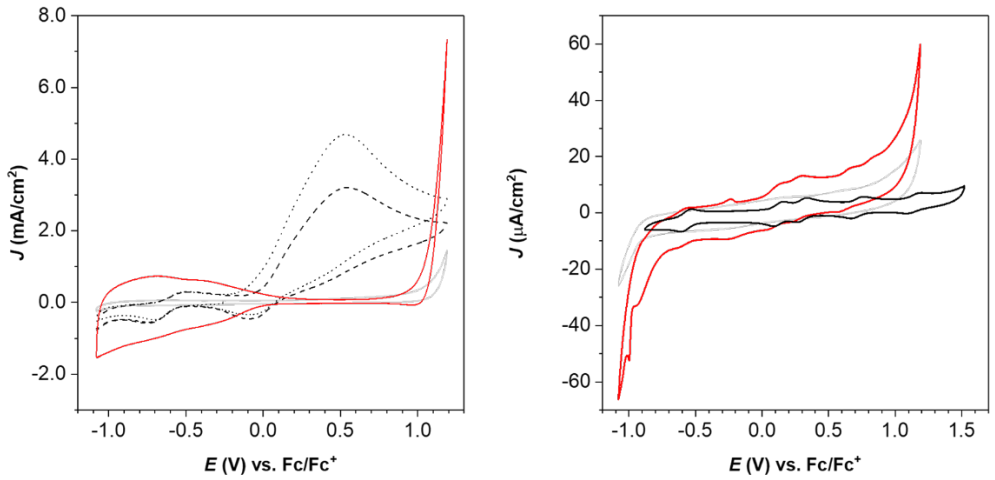

Figure S18. Electrochemical analysis of the electrode and of the solution after the CPE at 1.19 V, referred to Figures 4 and S17. Left, black dotted trace, first CV cycle of $\mathbf{Fe_5}^{3+}$ 0.2 mM dissolved in 10:1 MeCN:H_2O before CPE experiment (Figure S17) using ITO as WE, at a scan rate of 100 mV/s (V_i = V_f = -1.08 V; V_{C1} = 1.19 V). Black dashed trace, second CV cycle. Red trace, CV of the ITO working electrode obtained after CPE in Figures S17, immersed in a clean electrolyte solution. Gray trace, CV of a bare ITO electrode under the same conditions. ITO electrode (S = 2 cm^2) (WE), Pt mesh (CE), Ag/Ag^+ (RE). Right, red trace, CV of $\mathbf{Fe_5}^{3+}$ 0.2 mM dissolved in 10:1 MeCN:H_2O after CPE experiment (Figure S17) using a GC working electrode, at a scan rate of 100 mV/s (V_i = V_f = -1.08 V; V_{C1} = 1.19 V). Black trace, CV of $\mathbf{Fe_5}^{3+}$ 0.2 mM dissolved in MeCN. Gray trace, CV of a bare GC electrode under the same conditions. GC (WE), Pt mesh (CE), Ag/Ag^+ (RE).

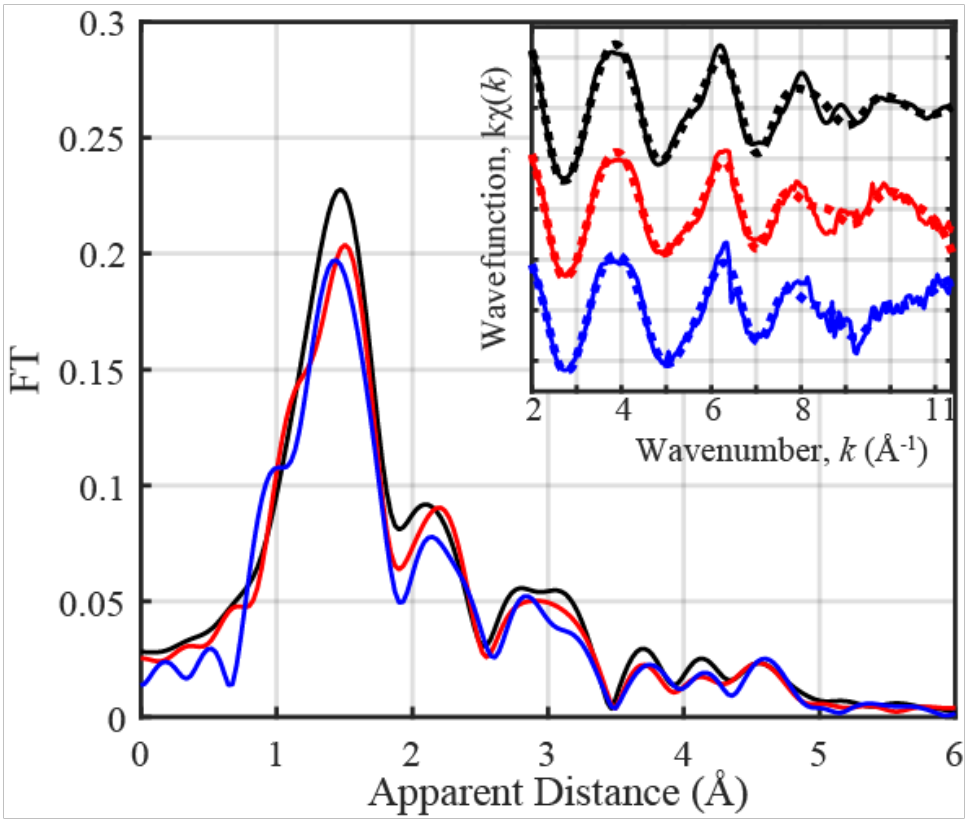

Figure S19. Experimental Fourier transforms of k-weighted Fe EXAFS, related to Figure 6. $\mathbf{Fe_5}^{3+}$ powder (black), $\mathbf{Fe_5}^{3+}$ dissolved in pure CH_3CN (red) and $\mathbf{Fe_5}^{3+}$ dissolved in CH_3CN: H_2O (10:1) (blue) together with EXAFS fits (Table S3) shown as an inset.

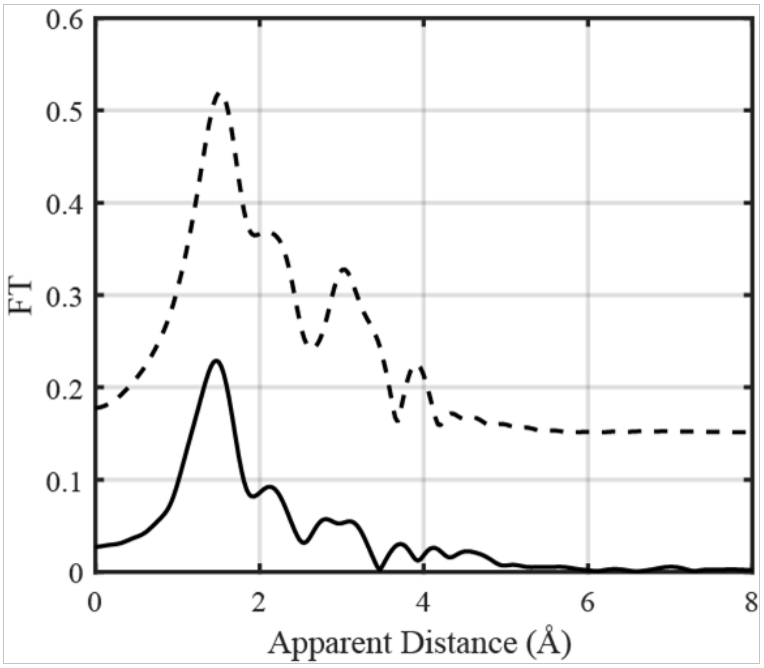

Figure S20. **Experimental Fourier transforms of k-weighted Fe EXAFS of Fe_5^{3+} powder (solid black line) and EXAFS spectra simulated with FEFF software (dashed black line), related to Figure 6**. for comparison. Coordinates of all atoms from X-ray structures (Koningsberger, D. C.; Prins, 1988) were used as input.

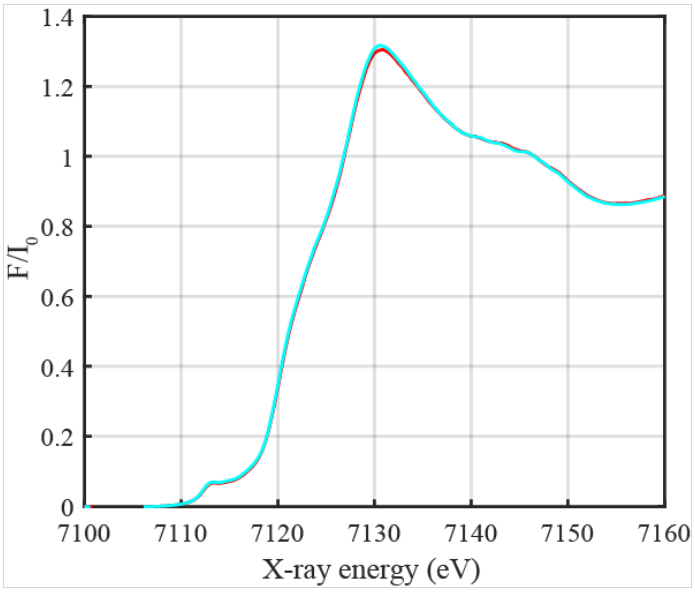

Figure S21. **Normalized Fe K-edge, related to Figure 6**. **Fe_5^{3+}** dissolved in pure CH_3CN (red) and **Fe_5^{3+}** dissolved in CH_3CN: H_2O (10:1) (cyan) frozen solution.

Transparent Methods

Materials

All the chemicals used in this work were provided by Sigma Aldrich and they have been used without further purification unless explicitly indicated. $FeSO_4 \cdot 7H_2O$ was purchased from Alfa-Aesar, 3,5-bis(2-pyridyl)pyrazole (Hbpp) was synthesized according to the published procedure (Dowling, Dinsdale and Lemaire, 2015). $[Fe^{II}_4Fe^{III}(\mu_3\text{-}O)(\mu\text{-}bpp)_6]$ $(BF_4)_3$, (**$[Fe^{II}_4Fe^{III}]^{3+}$** or **Fe_5^{3+}**), was synthesized following a methodology previously described in the literature (Okamura *et al.*, 2016). The solvents employed in this work were dried by a SPS® system and later degassed by bubbling nitrogen or argon before starting the reactions. All aqueous solutions used for electrochemical measurements were prepared with high purity de-ionized water obtained by passing distilled water through a nanopure Mili-Q water purification system. Glassy Carbon Disk (GC), Glassy Carbon Rod (GC_{rod}), Platinum Disk (Pt) and $Ag/AgNO_3$ were purchased from IJ-Cambria Ldt. Glassy Carbon Plates (Sigradur® K films 20 mm x 10 mm x 180 μm) were acquired from HTW Germany. Indium Tin Oxide (ITO) electrodes (Rs = 8−12 Ω) were purchased from ALPHA BIOTECH.

Instrumentation and Methods

Electrochemical measurements

Cyclic voltammetry (CV), Differential Pulse Voltammetry (DPV) and Controlled Potential Electrolysis (CPE) were carried out using a CHI660D potentiostat. Glassy carbon electrode (GC) (d = 3 mm), Glassy carbon Rod (GC_{rod}), Glassy carbon plate (GC_{plate}) or Indium Tin Oxide (ITO) electrode (S= 2 cm^2, Rs = 8−12 Ω) were employed as working electrode (WE). In case of Glassy carbon plate (GC_{plate}) or Indium Tin Oxide (ITO) the surface dipped in solution was 2 cm^2. Pt disk was employed as a counter electrode (CE) and $Ag/AgNO_3$ (0.01 M $AgNO_3$ in 0.1 M solution of $TBAPF_6$ in MeCN) as a reference (RE). Glassy carbon (GC) electrodes were polished with 1.0, 0.3 and 0.05 μm micron alumina paste, washed with distilled water and sonicated in acetone for 10 minutes before performing each experiment. All the potentials values reported in this work have been measured vs $Ag/AgNO_3$ reference electrode and converted to Fc/Fc^+ by adding ferrocene/ferrocenium as internal standard ($E_{1/2}(Fc/Fc^+) \approx 0.08$ vs $Ag/AgNO_3$) at the end of each experiment ($E_{1/2}(Fc/Fc^+) \approx + 0.548$ V vs NHE) (Addison and Pavlishchuk, 2000). All the electrochemical experiments carried out in acetonitrile

(MeCN) were performed with the presence of 0.1 M tetraethyl ammonium perchlorate (TEAP) as supporting electrolyte.

Cyclic voltammetry (CV), differential pulse voltammetry (DPV): CV measurements were conducted under an N_2 atmosphere, unless otherwise stated at room temperature (24−25 °C), in a three-electrode cell. The scan rate was set at 10 mV/s unless otherwise stated. DPV was collected with amplitude= 50 mV, step height=4 mV, pulse width= 0.05 s, pulse period= 0.2 s and sampling width= 0.0167 s.

Controlled potential electrolysis (CPE): CPE experiments were carried out under an N_2 atmosphere, unless otherwise stated at room temperature (24−25 °C) in a gastight, two-compartment, three-electrode cell. In this case, ITO (S = 2 cm^2) or GC_{rod} were used as working electrode and Pt mesh was used as a counter electrode.

O_2 detection by Clark electrode: During the CPE experiment, the oxygen evolution was monitored with an OXNP type Clark electrode in gas phase (from Unisense Company). This electrode was positioned in the headspace of the compartment cell where the WE and the RE are placed. The oxygen was removed by bubbling nitrogen during 30 min. Once the Clark signal reached values close to 0 mV, the nitrogen flow was stopped and the base line was left to stabilize. The CPE was started once the oxygen sensor signal was stable. The experiment was performed under vigorous stirring. Calibration of the oxygen sensor was done by adding known amount of pure oxygen into the cell using a gas tight Hamilton syringe. The blank experiment followed the same procedure. The Faraday efficiency was determined according to the total charge passed during the CPE and the total amount of generated oxygen by considering that water oxidation is a 4 e^- oxidation process.

Solid State characterization of the electrodes.

SEM and EDX analyses were carried out on a JEOL JSM 6700F electron microscope working at 10 kV. XPS experiments were performed with a SPECS EA10P hemispherical analyser using a non-monochromated X-ray source (Al Kα line of 1486.6 eV and 300W). The direction of the X-ray source

with respect to the sample was 90º and ultrahigh vacuum was maintained during the measurements, obtaining a residual pressure of 10^{-8} Pa.

Preparation of the electrodes: GC_{rod} electrodes (d= 3 mm), used for SEM and XPS analysis, were cut in pieces 4 mm tall. The pieces were left in 6 M H_2SO_4 aqueous solution overnight to avoid possible traces of metals during the measurements. Afterwards, they were sonicated in Milli-Q water for 30 min, polished with 1.0, 0.3 and 0.05 micron alumina paste, washed with distilled water and sonicated in acetone for 10 minutes. The experiments were performed covering the side of the electrode and leaving exposed only the top surface (S = 0.07 cm^2). The ITO glass slides (2 cm^2) were immersed in the electrolyte solution and sonicated in MeOH (K_2CO_3 sat.) for 30 min and then rinsed with acetonitrile and water(Okamura *et al.*, 2016).

UV-vis spectrometry

UV-vis spectrometry was performed using a Cary 50 (Varian) UV-vis spectrophotometer.

X-ray Absorption Spectroscopy (XAS) Methods.

X-ray absorption spectra were collected at the CLAESS beamline at the ALBA synchrotron light source (Simonelli *et al.*, 2016). The radiation was monochromatized using a pair of Si(111) crystals. The intensity of the X-rays were monitored by three ion chambers (I_0, I_1 and I_2). I_0 placed before the sample was filled with 100% nitrogen while I_1 and I_2 placed after the sample were filled with 77 % N_2 and 23 % Kr. Fe metal was placed between ion chambers I_1 and I_2 and its absorption was recorded with each scan for energy calibration. The samples were measured in customized PEEK sample holders and measured with a defocused beam spot size of 500 x 500 µm using a liquid nitrogen cryostat cooled down to 77 K. Fluorescence absorption measurements were carried out with an Amptek silicon drift solid state detector (XR-100 SDD)(Simonelli *et al.*, 2016) placed at 90 degrees to the incoming beam. The silicon drift detector was placed on a motorized stage allowing the sample-detector distance to be easily changed between 30-110 mm (Koningsberger, D. C.; Prins, 1988). Solid Fe_2O_3 diluted with BN powder, was pressed between kapton and mylar tape, and measured in the cryostat in transmission mode. Around 3 scans were collected on Fe_2O_3 and around 20-25 scans were collected on the solution and hybrid samples. Care was taken to measure at different spots on

both the solution and hybrid samples in order to minimize radiation damage. No more than 2 scans were taken in this instance on each spot on the solution samples. All samples were also protected from the x-ray beam during spectrometer movements by a shutter synchronized with the scan program. Fe XAS energy was calibrated by the first maxima in the second derivative of the iron metal X-ray absorption near edge structure (XANES) spectrum.

Extended X-ray Absorption Fine Structure (EXAFS) Analysis

Athena software (Ravel and Newville, 2005) was used for data processing. The energy scale for each scan was normalized using copper metal standard. Data in energy space were pre-edge corrected, normalized, deglitched (if necessary), and background corrected. The processed data were next converted to the photoelectron wave vector (k) space and weighted by *k*. The electron wave number is defined as $k = [2m(E - E_0)/\hbar^2]^{1/2}$, E_0 is the energy origin or the threshold energy. K-space data were truncated near the zero crossings k = 2 to 11.375 Å^{-1} for the solid, solution and hybrid complexes, in Fe EXAFS before Fourier transformation. The k-space data were transferred into the Artemis Software for curve fitting. In order to fit the data, the Fourier peaks were isolated separately, grouped together, or the entire (unfiltered) spectrum was used. The individual Fourier peaks were isolated by applying a Hanning window to the first and last 15% of the chosen range, leaving the middle 70% untouched. Curve fitting was performed using *ab initio*-calculated phases and amplitudes from the FEFF8 (Rehr, Albers and Zabinsky, 1992) program from the University of Washington. *Ab initio*-calculated phases and amplitudes were used in the EXAFS equation

$$\chi(k) = S_0^2 \sum_j \frac{N_j}{kR_j^2} f_{eff_j}(\pi, k, R_j) e^{-2\sigma_j^2 k^2} e^{\frac{-2R_j}{\lambda_j(k)}} \sin(2kR_j + \phi_{ij}(k)) \qquad \text{(S2)}$$

where N_j is the number of atoms f_{effj} in the j^{th} shell; R_j the mean distance between the absorbing atom and the atoms in the j^{th} shell; (π,*k*, R_j) is the *ab initio* amplitude function for shell *j*, and the Debye-Waller term accounts for $e^{-2\sigma_j^2 k^2}$ damping due to static and thermal disorder in absorber-backscatterer distances. The mean free path term $e^{\frac{-2R_j}{\lambda_j(k)}}$ reflects losses due to inelastic scattering, where $\lambda_j(k)$, is the electron mean free path. The oscillations in the EXAFS spectrum are reflected in the sinusoidal term $\sin(2kR_j + \phi_{ij}(k))$, where $\phi_{ij}(k)$ is the *ab initio* phase function for shell

j. This sinusoidal term shows the direct relation between the frequency of the EXAFS oscillations in k-space and the absorber-backscatterer distance. S_0^2 is an amplitude reduction factor.

The EXAFS equation (Simonelli *et al.*, 2016) (Eq. S2) was used to fit the experimental Fourier isolated data (q-space) as well as unfiltered data (k-space) and Fourier transformed data (R-space) using *N*, S_0^2, E_0, *R,* and σ^2 as variable parameters (Table S3). *N* refers to the number of coordination atoms surrounding Fe for each shell. The quality of fit was evaluated by R-factor and the reduced Chi^2 value. The deviation in E_0 ought to be less than or equal to 10 eV. R-factor less than 2% denotes that the fit is good enough. R-factor between 2 and 5% denotes that the fit is correct within a consistently broad model. The reduced Chi^2 value is used to compare fits as more absorber-backscatter shells are included to fit the data. A smaller reduced Chi^2 value implies a better fit. Similar results were obtained from fits done in k, q, and R-spaces.

X-Ray Crystallography

Crystal preparation: Crystals of **$[Fe^{II}_2Fe^{III}_3]^{5+}$** were grown by slow evaporation of acetonitrile in ethyl ether, from a solution after the CPE at 1.19 V. The crystals were selected using a Zeiss stereomicroscope using polarized light and prepared under inert conditions immersed in perfluoropolyether as protecting oil for manipulation.

Data collection: Crystal structure determination for sample **$[Fe^{II}_2Fe^{III}_3]^{5+}$** was carried out using a Apex DUO Kappa 4-axis goniometer equipped with an APPEX 2 4K CCD area detector, a Microfocus Source E025 IuS using MoK_α radiation, Quazar MX multilayer Optics as monochromator and an Oxford Cryosystems low temperature device Cryostream 700 plus (T = -173 ˚C). Full-sphere data collection was used with ω and φ scans. *Programs used:* Bruker Device: Data collection APEX-2 (Bruker, 2007a), data reductiesion Bruker Saint (Bruker, 2007b) V/.60A and absorption correction SADABS (Blessing, 1995; Bruker, 2001).

Structure Solution and Refinement: Crystal structure solution was achieved using the computer program SHELXT (Sheldrick, 2015a). Visualization was performed with the program SHELXle (Huebschle, Sheldrick and Dittrich, 2011). Missing atoms were subsequently located from difference Fourier synthesis and added to the atom list. Least-squares refinement on F^2 using all measured intensities was carried out using the program SHELXL 2015 (Sheldrick, 2015b). All non-hydrogen atoms were refined including anisotropic displacement parameters.

Supplemental References

Addison, V. V. P. A. W.; Pavlishchuk, V. (2000). Conversion Constants for Redox Potentials Measured versus Different Reference Electrodes in Acetonitrile Solutions at 25°C. Inorganica Chim. Acta *298 (1)*, 97–102.

Blessing R. H. (1995) An empirical correction for absorption anisotropy. Acta Cryst. *A51*, 33-38.

SADABS: V2012/1 Bruker (2001). Bruker AXS Inc.

Data collection with APEX II version v2013.4-1. Bruker (2007a). Bruker AXS Inc.

Data reduction with Bruker SAINT version V8.30c. Bruker (2007b). Bruker AXS Inc.

Dowling, C.; Dinsdale, D. R.; Lemaire, M. T. (2015). Complexes of Imidazole- or Pyrazole-Substituted Ligands. Can. J. Chem. *93*, 769–774.

Huebschle, C.B.; Sheldrick, G.M.; Dittrich, B. (2011). ShelXle: a Qt graphical user interface for SHELXL. *J.* Appl. Cryst. *44*, 1281-1284.

Koningsberger, D. C.; Prins, R. *X Ray Absorption: Principles, Applications, Techniques of EXAFS, SEXAFS and XANES*; John Wiley & Sons, 1988.

Ravel, B.; Newville, M. (2005). J. Synchrotron Radiat*. 12*, 537.

Rehr, J. J.; Albers, R. C.; Zabinsky, S. I.(1992). Phys. Rev. Lett. *69*, 3397.

Simonelli, L.; Marini, C.; Olszewski, W.; Ávila Pérez, M.; Ramanan, N.; Guilera, G.; Cuartero, V.; Klementiev, K. (2016). Cogent Physics. *3*, 1231987

Sheldrick, G. M. (2015a). SHELXT – Integrated space-group and crystal-structure determination. Acta Cryst. *A71*, 3-8.

Sheldrick, G.M. (2015b). Crystal structure refinement with SHELXL. Acta Cryst*. C71*, 3-8.